The Aerodynamic Consequences on Wheels due to Tyre Deformation under Operating Conditions

MACQUARIE
University
SYDNEY·AUSTRALIA

Sajjad Saleh

Faculty of Science and Engineering

Master of Research

Supervised by

Dr Sammy Diasinos

Submitted: May 1, 2018

Statement of Originality

I, Sajjad Saleh hereby declare that this thesis submission is my own work and has not previously been submitted for a degree or diploma in any university. To the best of my knowledge and belief, the thesis contains no material previously published or written by another person except where due reference is made in the thesis itself.

Signed: _____

Date: 01/05/2018

Acknowledgements

Firstly I would like to acknowledge and thank the efforts of my supervisor Dr Sammy Diasinos for not only his efforts during my thesis, but also his efforts for the majority of my time at Macquarie University. I would not be in the position I am in now if it weren't for his guidance and relentless will to expand my knowledge. His knowledge of CFD and aerodynamics proved to be a great help to me during this thesis. He was always making time for me when I needed it and never showed any remorse when I asked for assistance.

I would also like to thank my friends who have been and are going through the process that I am going through now. James has been incredibly supportive of me and has always been very quick to give me any assistance I required. He also made himself available for my morning coffee drinking sessions, making sure the day started the best it could. I also want to thank Andre Fellipe Vilanova de Araujo Aquino for always making yourself available for my afternoon coffee drinking sessions, making sure the day ended the best it could. I would like to thank Liang Yu as well, for being the comedic relief during my thesis, you kept my spirits high.

Finally, I would like to thank all my other friends who helped support me during my thesis, especially Tim Jellema. Whether it was grabbing lunch or dinner or even spending the nights with me gaming, you guys kept my spirits high and made sure I performed the best I could.

Abstract

The aerodynamic performance of a vehicle is a key attribute that affects its fuel efficiency. The wheels of a vehicle contribute approximately 30% of its total aerodynamic drag, therefore understanding key flow structures is vital in the hopes of improving overall vehicle fuel efficiency. A detailed review has been presented on the operating conditions of wheels as well as the deformation this causes to the contact patch and sidewall of a tyre. This study presents five tyres based off Fackrell's A2 wheel with either centrifugal growth, increased vertical loading or asymmetric loading. It was seen that the growth of the sidewall increases the strength of the two main vortices produced at the contact patch of the wheel. These wheels also saw a reduction of drag by 3-10% and reduction of lift by 11-26%. Increased vertical loading reduced the strength of the two main vortices, with extreme loading restricting their formation. The drag reduction from minor loading was negligible, however lift increased by 14%. Major loading resulted in a drag and lift reduction of 18% and 13% respectively. The wheel with both centrifugal growth and increased vertical loading saw no variation in lift and drag.

Table of Contents

List of Figures

List of Tables

Nomenclature

ρ	Density
P	Pressure
$\vec{u}$	Velocity magnitude
u	Velocity
v	Velocity
w	Velocity
C_L	Coefficient of Lift
C_D	Coefficient of Drag
C_P	Coefficient of Static Pressure
C_{TP}	Coefficient of Total Pressure
ω	Specific Dissipation Rate
ε	Dissipation Rate of Turbulent Kinetic Energy
k	Turbulent Kinetic Energy
D	Wheel Diameter
μ	Dynamic Viscosity
θ	Angular Position on Wheel Surface
δ	Boundary Layer Thickness
l	Reference Length
CAD	Computational Aided Design
CFD	Computational Fluid Dynamics
RANS	Reynolds Averaged Navier-Stokes
Re	Reynolds Number
GCI	Grid Convergence Index

1 Introduction

1.1 Background and Motivation

In recent times there has been a large push in the car industry to make their vehicles as fuel efficient as possible. This is not only to reduce the everyday cost for the general public but also the reducing the impact that cars have on the environment. A prime method to improve the fuel efficiency of a vehicle is to reduce the aerodynamic drag. By reducing the amount of drag produced by a vehicle, the amount of resistance force it feels at a given velocity is significantly reduced, thus reducing the power requirements for the vehicle. Studies have shown that the airflow around the wheels of a car contributes to 30% of its overall drag value [1]. This contribution to the drag number of a vehicle is significant and it showcases the importance to understand the flow features of a wheel under realistic operating conditions.

The wheels of a car affect the aerodynamic drag produced due to the fact that they create large areas of turbulent flow downstream as well as creating recirculation zones in the wheelhouses using the air that passes from the underside of the car [2]. Creating isolated simulations of objects improves the understanding of key flow structures by reducing the number of disturbances that the flow would face. With this greater understanding of key flow structures, the influence of certain geometric variations can be quantified with an increased level of accuracy. Once this understanding is gained, it is then possible to advance the problem to include items such as wheelhouses and potentially full scale vehicle testing.

Various studies have been conducted on static wheels, rotating wheels and even yaw and camber adjusted wheels. While these conditions do replicate what the wheel experiences under normal running well, they do not tell the whole story. Studies have shown that the geometry of tyres significantly changes due to their operating conditions. The inflation pressure, rotational velocity and weight of the vehicle all deform the tyre in various separate ways. Even the setup of wheels, such as camber and toe, change the way they tyre structure reacts to forces. Studies have shown that the contact patch of a wheel is a key area for the creation of drag inducing flow, it is, therefore, critical to understand how deformation of the tyre affects not only the contact patch shape but also key flow structures associated with wheels [3].

This thesis will attempt to generate an understanding of what the aerodynamic consequences on wheels are due to tyre deformation that is expected to be present during the normal operation of a vehicle.

1.2 Literature Review

1.2.1 Aerodynamic Studies on Wheels

1.2.1.1 Isolated Wheel Studies

Aerodynamic studies of isolated wheels have been a heavily investigated field with researchers acknowledging that the flow structures generated from wheels have large implications for various other components of a vehicle. Investigations began with a study on an isolated racing wheel by Morelli in 1969 [4]. The wheel was placed on a stationary ground with a 15mm recess to allow the wheel to rotate freely tangentially to the free steam. The recess was created to portray the deformation the tyre experiences from the weight of a vehicle without ever being in contact with the ground. Given that the wheel was never in contact with the ground, Morelli was able to use a force balance to measure the lift and drag. The lift and drag coefficients were calculated to be -0.1 and 0.5 respectively at a Reynolds number of $1.3x10^6$ [4]. Morelli's results contradicted the widely reported opinion that wheels should produce lift. This raised questions about his decision to include a gap between wheel and the ground.

Cogotti later proved that the venturi effect did negatively influence Morelli's results by creating experiment of a rotating wheel with changing ground clearances [5]. Similar to Morelli, Cogotti utilised a stationary ground, however, there was no recess present and instead, a foam block was placed under the wheel. An AC motor was used to rotate the wheel, Cogotti mentioned that the placement of the motor did influence the results of the experiment, however, would not affect any major trend present [5].

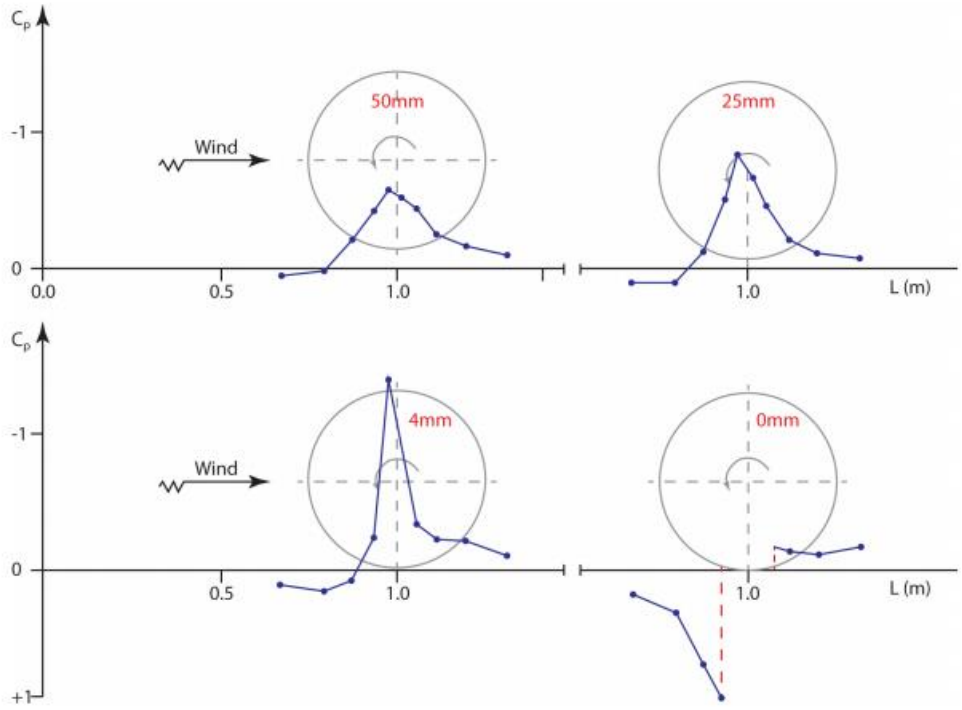

Figure 1.1: Pressure distribution over a rotating wheel with varying ground heights (modified by Sprot [6]) [5].

Cogotti placed the wheel with ground clearances of 50mm, 25mm, 4mm and 0mm and measured the surface pressure distribution along the centre circumference of the wheel as seen in the Figure 1.1. It was found that there was a small spike in negative C_p with the ground clearance at 50mm. This spike then increased as the wheel moved closer to the ground. However, the inverse occurred with no ground clearance. A large positive C_p spike was observed near the contact between the wheel and the ground [5]. This resulted in a lift producing wheel, thus proving the venturi effect taking place in Morelli's experiment. Cogotti's experiment showcases the importance of the contact between the wheel and ground.

Fackrell created a series of experiments measuring the lift and drag of various grand prix inspired wheels of differing widths (A=0.46D, B=0.61D and C=0.81D) and shoulder profiles (1 and 2), all with a diameter of 416mm [7]. However, rather than using pneumatic wheels, the wheels were solid and made out of aluminium. This ensured that the wheels would not deform in any way, thus only the parameters that were varied would cause variations in results [7]. Fackrell placed emphasis on modelling the wind tunnel conditions similar to what the wheels would experience on the track. In general, racing car wheels experience conditions with Reynolds Number between $5x10^5$ and $2.5x10^6$ based on the diameter of the wheels. Thus all experiments were run with a Reynolds number of $5.3x10^5$ by ensuring the free stream velocity inside the wind tunnel remained at $18.6ms^{-1}$ for all wheels tested [7]. Fackrell ensured that the wheels were in contact with the ground, thus not allowing the use

of a force balance to measure the lift and drag of the wheels. In order to measure the forces on the wheel, Fackrell took a series of static pressure readings on the surface of the wheel which were then integrated to calculate lift and drag.

Fackrell initially compared the lift and drag forces of a rotating and stationary B2 with a moving and stationary ground respectively. Fackrell found that the lift and drag of the rotating B2 were approximately 42% and 25% lower than that of the stationary wheel, with lift and drag coefficients of 0.44 and 0.76 respectively. The reasoning for this reduction can be seen through the static pressure plotted along the centreline of the wheel showcased in Figure 1.2. The coefficient of pressure measured at the contact patch showed large variations between the two cases. The rotating case experiences a peak coefficient of pressure greater than two whereas the stationary case experiences a value of approximately one. Fackrell explains that the pressure value obtained at the contact patch is so great due to the viscous forces associated with the wheel and ground are converging to a singular point in front of the contact patch. This jetting action was then predicted to continue moving downstream down the side of the wheel, aiding in the formation of two primary vortices. However, the formation of the vortices was not proven by Fackrell.

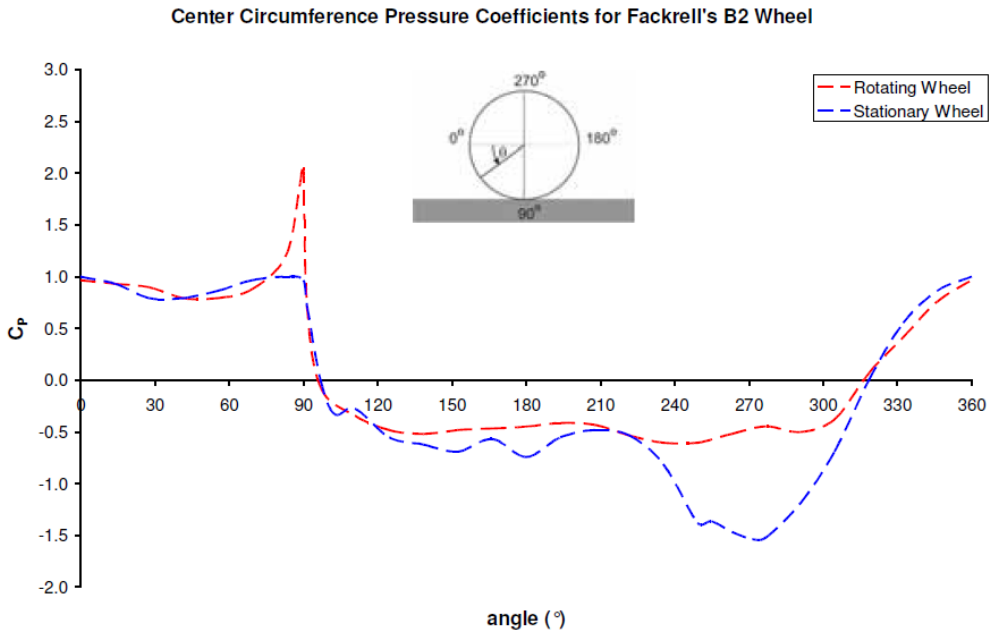

Figure 1.2: Static pressure distribution over a rotating and stationary B2 wheel [3] [7].

Another area of interest is the large peak in negative pressure at the separation point of the stationary wheel (approximately 270-300 degrees), this explains the increase in lift of the stationary wheel. The separation point itself is further forward on the rotating wheel, this is due to the opposing velocities of the surface of the wheel and the free stream at that given point. Fackrell mentioned that although

he was not able to measure it, there is expected to be a large negative pressure peak directly behind the contact patch. This was later confirmed to be the case in later experiments by Mears in 2004 [8].

Comparing the different widths of wheels, Fackrell found that the drag coefficient of the narrow A2 wheel expectably was reduced by 36% with a lift coefficient reduction of 12%. Conversely, the C2 wheel saw an increase in the drag coefficient of 21% with a reduction in lift coefficient of 2%. Fackrell mentioned doubts about the measurement of the forces of the B2 wheel, explaining the lack of correlation. However, measurement techniques used to visualise the wake flow was constant between all different wheel geometries. Comparing the different shoulder profiles, it was determined that the B2 wheel experienced a lift coefficient increase of approximately 10% and a reduction of drag coefficient of 8% versus the B1 wheel. It should be noted that the other variations of wheels showcased no accountable change in lift and drag coefficients between their different shoulder counterparts. This again raised questions about the accuracy of the force measurements of the B2 wheel.

By comparing the pressure distribution on the surface of the A1 and A2 wheels, certain conclusions can be made. It was observed that the change in shoulder profile made no effect on the pressure distribution at the centreline of the wheel, the lift and drag coefficients of the two wheels were calculated to be identical. However, moving away from the centreline to the first point the wheel is not in contact with the ground, the A1 wheel sees higher peak pressure values compared to the A2 wheel suggesting that while the overall lift and drag values may be unchanged, the flow structures generated from the sidewalls are affected by small geometric changes. Therefore further research is necessary to determine how these changes in pressure distribution affect the flow structures associated with wheels. To add to this, the A1 and A2 wheel had identical tread widths, thus the contact patch did not vary. This opens another area of potential research, as the contact patch is key to the formation of flow structures.

One such flow structure was identified by Bearman et al. in 1998, after initially being predicted by Fackrell [9]. The flow structures in question were the two primary vortices that are formed by the jetting action both in front and to the sides of the contact patch. To prove the existence of primary vortex structures associated with wheels and to further exemplify the importance of accurate ground representation, Bearman et al. conducted wind tunnel experiments using the same apparatus as Fackrell. However, Bearman implemented the use of a nine-hole pressure probe in the wake region of the wheel, to aid in the visualisation of key flow structures, as well as using both a moving and stationary ground. Using the pressure probe, it was observed that these vortices travelled further

downstream with the stationary wheel rather than the rotating wheel and were positioned further apart and closer to the ground [9]. As a result, the rotating wheel showed a taller wake region. Bearman also found that the presence of the moving ground greatly affected results. It is believed that the momentum loss associated with stationary grounds greatly affect the flow structures in close proximity, thus leading to incorrect lift and drag measurements. Even using methods such as tangential blowing of air across a stationary ground to mimic the no-slip condition of a moving ground still influenced the wake structure. Thus Bearman concluded that for any aerodynamic research in close proximity to a ground, a moving ground must be used for meaningful results [9].

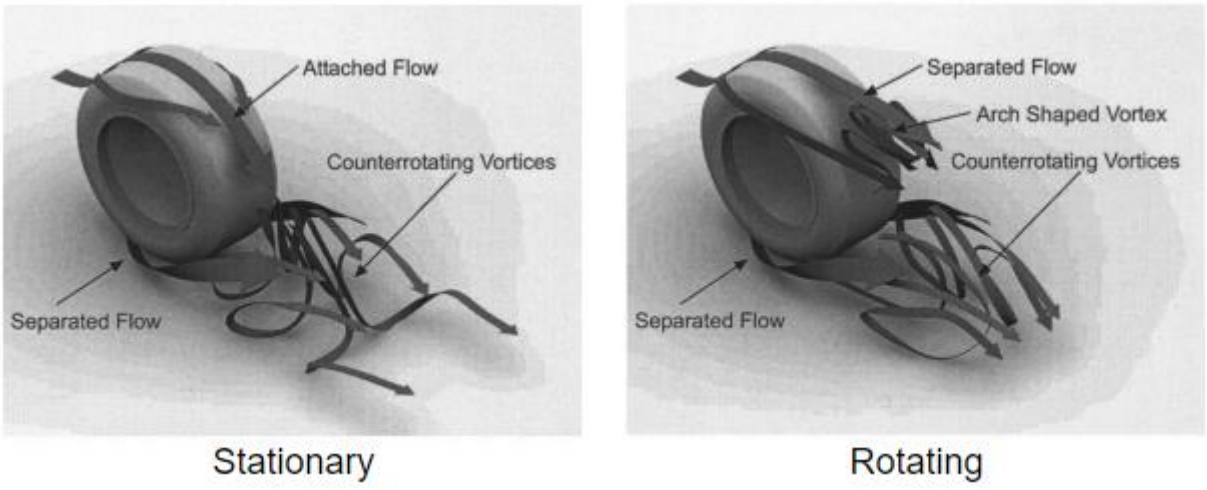

Figure 1.3: Flow structures associated with stationary and rotating wheels [10].

To further understand the differences in flow structures between stationary and rotating wheels, McManus and Zhang conducted a series of CFD simulations. Their results showcasing the flow structures is presented in Figure 1.3. Immediately they noticed significant variations in the flow structures forming at the top of the wheel near the separation point. They believe that the reason that the wake of the rotating wheel is taller is due to the fact that the early separation of flow for the rotating wheel causes the creation of arch-shaped vortices that do not interact with the lower counter-rotating vortices [10]. McManus and Zhang suggested that the wake of the stationary wheel was wider and lower due to the stationary ground. They stated that the boundary layer growth deflected flow less than on moving grounds, resulting in the lower and wider wake region.

McManus and Zhang's visualisation of the flow associated with wheels outlined the formation of another key vortex structure. The earlier separation of flow for the rotating wheel formed two secondary vortices at either side of the top of the wheel. The significance of these vortices were dismissed by McManus and Zhang, stating that these vortices did not influence the structure of the primary vortices [10].

However, McManus and Zhang's claims were proven to be incorrect by further studies conducted by Diasinos in 2009 [3]. Diasinos conducted four CFD simulations on rotating and stationary wheels using Fackrell's A2 design. The four cases tested were a complete rotating wheel, a wheel with only the top half rotating, a wheel with only the bottom half rotating and a complete stationary wheel [3]. Figure 1.4 illustrates this.

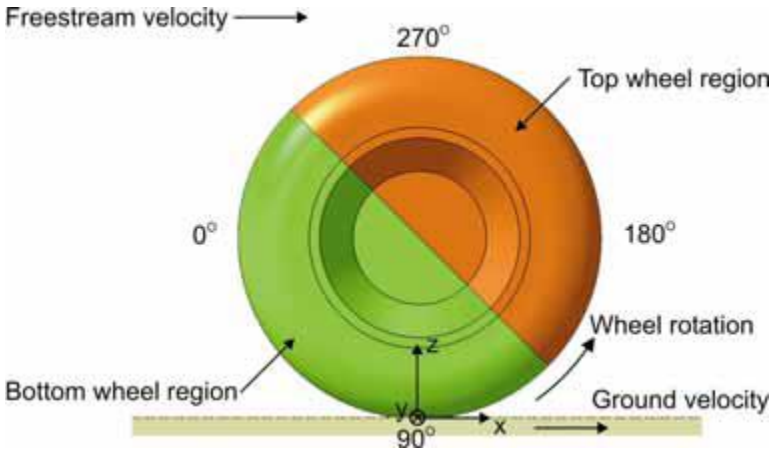

Figure 1.4: The method in which the wheel was split for top and bottom wheel rotation [3].

Diasinos found that the early separation due to the rotation of the top surface and the increase in strength of the two secondary vortices is the cause of the two counter-rotating vortices being formed higher and in a more central position. Diasinos believed that the early separation of flow over the top of the wheel resulted in the removal of the downwash in the central wake region, present in the stationary wheel, and replaced it with an increase in entertainment from the sides of the wheels [3].

Given that majority of isolated wheel testing was conducted on non-deformable aluminium wheels, Mears outlined the need to use pneumatic wheels for accurate wind tunnel testing in 2004 [8]. Mears used a similar more advanced and accurate method to Fackrell to take surface pressure readings on a pneumatic go-kart wheel. Rather than using pressure probes to map the wake structure of the wheel, Mears utilised particle image velocimetry (PIV), in order to receive much higher resolution of data, creating a more accurate visualisation of wake structure without intruding on the airflow [8].

Mears observed similar characteristics of his pneumatic wheel to that seen by Fackrell on his aluminium wheel. Comparing the C_p plots along the centreline of both wheels, the similarities between each case can be seen. Both wheels share the same positive pressure peak, stagnation point and flow separation point over the top of the wheel [8]. Interestingly, Mears' system of taking pressure measurements found the negative pressure peak directly behind the contact. This phenomenon was suggested to be the case by Fackrell, however, his methods were unable to see this trend. However, it should be mentioned that Mears did not provide a detailed analysis on the deformation the tyre

experienced during testing, therefore Fackrell's is a more desirable source to validate CFD simulations against, as the solid aluminium wheel provides fewer unknown parameters.

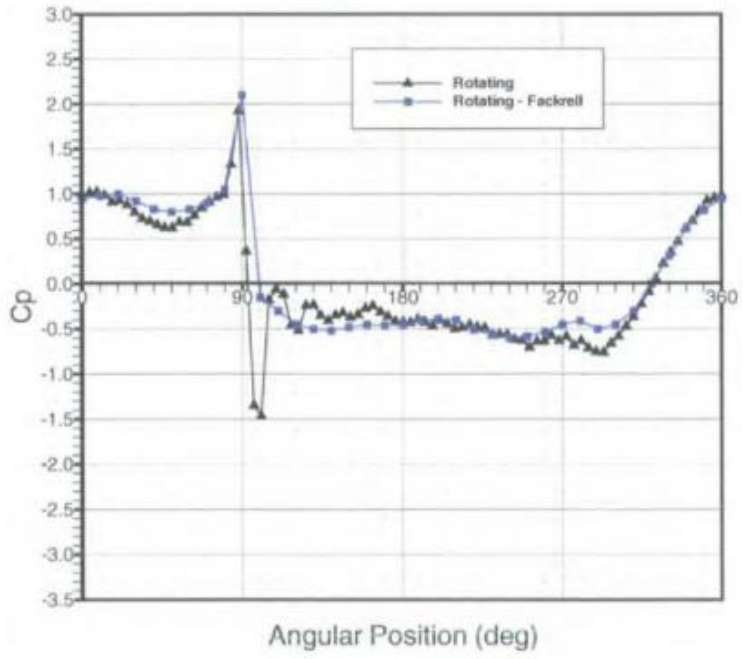

Figure 1.5: Static pressure distribution of Mears' pneumatic wheel versus Fackrell's A2 wheel [8].

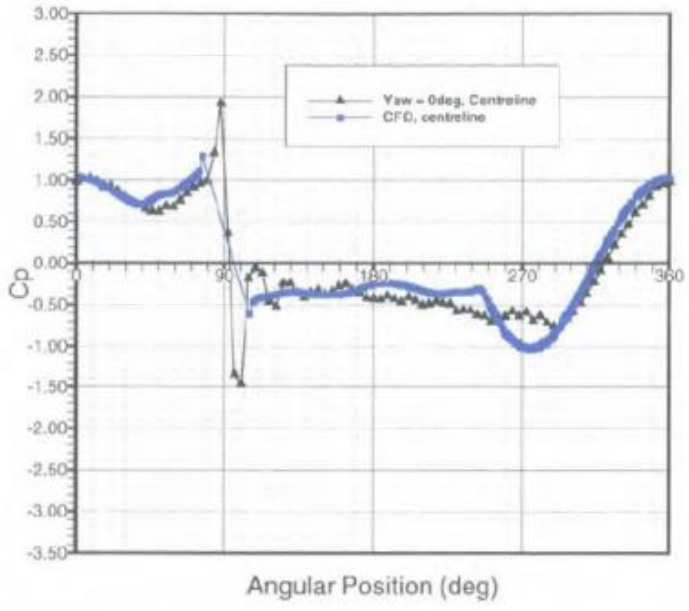

Figure 1.6: Coefficient of pressure plot about the centreline comparing experimental and computational data [8].

Nevertheless, Mears proceeded to conduct CFD simulations on his wheel using a tetrahedral mesh method. The wheel used in the CFD simulation was a simplified version of the go-kart wheel used in the wind tunnel testing, essentially the same sidewall shape but without hubs. Mears utilised both the

standard and RNG k-ε models, however, it was concluded that the standard model was more stable and was selected for the majority of the simulations.

Figure 1.6 showcases the C_p plots about the centreline of the wheel. It can be seen that the software was able to model the flow separation point over the top of the wheel accurately, however, both the positive and negative peak in C_p at the contact patch was under-predicted. This result raises two questions on the methods used by Mears. The results suggest that the contact patch was either not created geometrically correct or the mesh density in this region was far less than required.

Given that the Fackrell jetting phenomenon is a key area of study in the wake of a tyre, it is imperative to model the contact patch with high levels of accuracy in computational studies, as this region is directly connected to the formation of the two primary vortex structures. Poor modelling of this region has been shown to influence the results of simulations, as was seen from Mears' CFD simulations [8]. The main issue with meshing the contact patch for CFD simulations is that this region is essentially two bodies, the wheel and the ground, merging tangentially. This forces the mesh to be highly skewed at this point, leading to unstable and potentially inaccurate simulations. Diasinos in 2009 presented simplifications to the contact patch geometry allowing the mesh quality to be preserved [3].

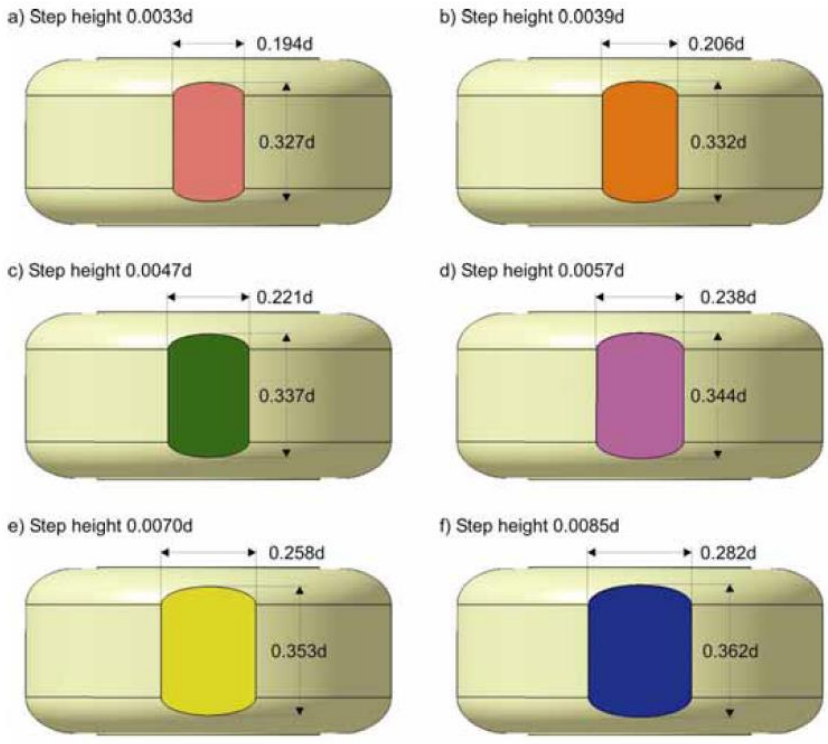

Figure 1.7: Cross section of the contact patch area of various step heights [3].

Initially, a plane parallel to the ground of a height that is a percentage of the wheel diameter is created. The wheel is then able to be trimmed at this level. The trim leaves a flat surface at the bottom of the wheel which is then extruded back to the ground plane, Figure 1.7 showcases the cross-sectional area of the newly created contact patch of varying plane step heights.

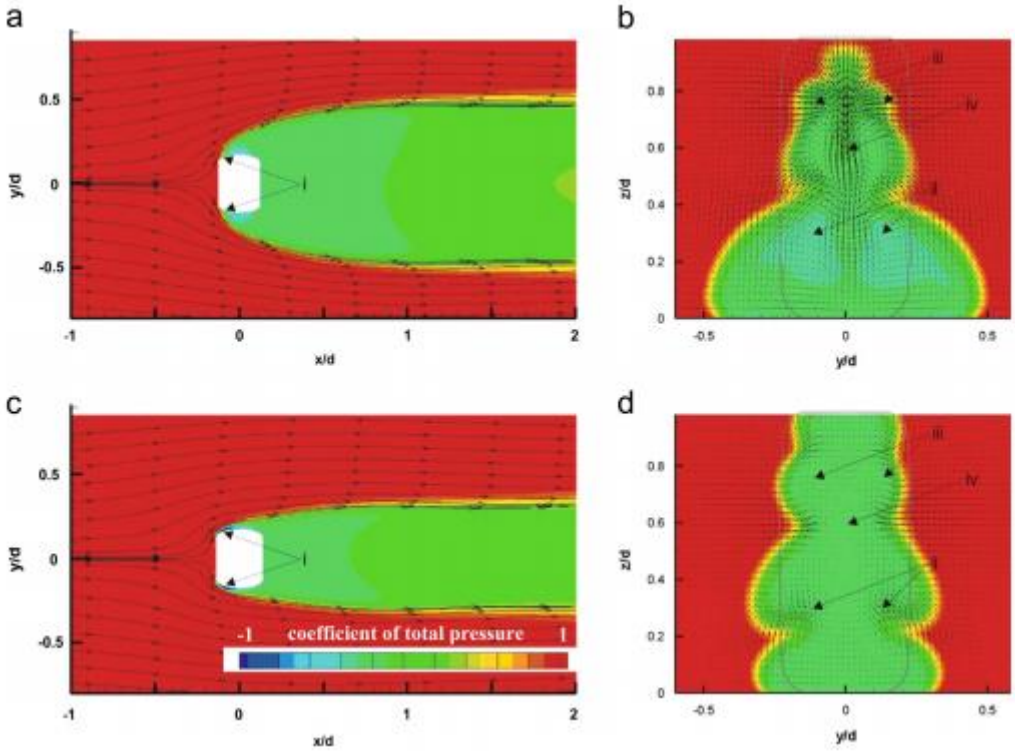

Figure 1.8: Coefficient of total pressure with varying contact patch step heights. (a) Step height=0.0028D at z/D=0.015 (b) step height=0.0028D at x/D=0.64 (c) step height=0.0085D at z/D=0.015 (d) step height=0.0085D at x/D=0.64 [11].

Figure 1.8 depicts the effect of varying the contact patch step height. It was seen that increasing the step height of the contact patch made the two primary vortices generated from this region less pronounced, resulting in a narrower and taller wake structure. These results are consistent with Fackrell's explanation of how the separation due to the jetting action at the contact patch causes the creation of these two vortices. It can be seen that increasing the step size delays this separation thus resulting in a reduction in the strength of these two vortices. Therefore, Diasinos concluded that the smallest step size of 0.0028d was best suited for simulations going forward, as this step height would cause the least variance in results whilst still being capable of generating meshes with low skewness values.

Further study was conducted on more recent wheel aerodynamics literature. However, detailed reviews of these has not been given as they were deemed not to be critical in the formation of the methodology of this study. This is primarily due to the fact that these recent studies delve into topics that deviate from what is being studied in this body of work. These topics include but are not limited

to yaw studies, rim and tyre modelling, wheel housing analysis, transient simulations with full car models, CFD rotation models for wheels and rims etc. Given the primary goal of this thesis is to understand the effects of tyre deformation on aerodynamic performance in an isolated scenario without the inclusion of parameters such as yaw. The inclusion of these papers do indicate the direction in which tyre aerodynamics is travelling in as well as where current knowledge stands [12-22].

1.2.2 Geometric Changes of Wheels

Wheels are exposed to a variety of geometric changes whilst they are under operating conditions [23]. Toe angle, camber angle, tyre pressure and slip ratio can affect the overall geometric changes that it undergoes when a certain load is applied to it. Given that the tyres are the only contact point between a vehicle and the road, these loadings can be very large and cause significant deformation in the sidewall and contact patch of the tyre. Therefore it is important to understand the structure of tyres and how they react to certain loading parameters.

1.2.2.1 Tyre Mechanics

Pneumatic tyres have a complex and varying construction that makes it very difficult to solve for deformation analytically using Finite Element Analysis (FEA) [24]. Whilst it is possible to create a spring body that mimics the dynamics of tyres, creating transient FEA simulations requires higher levels of detail in the mechanics of tyres. Tyres have proven to be very sensitive to temperature change and their viscoelastic behaviour makes it difficult to obtain consistent results in its deformation. To add to this point, there is a great chance that the velocity of the wheel can have a great effect on tyre deformation not only due to its motion but also due to the heat generation from the friction forces between it and the ground. These factors can result in irregular and inconsistent deformations that are difficult to simulate with accuracy [24]. To illustrate this point further, the contact patch would be the most likely position for large variations in temperature, and as will be discussed in later sections, the contact patch is a key area in regards to the aerodynamic performance of a wheel.

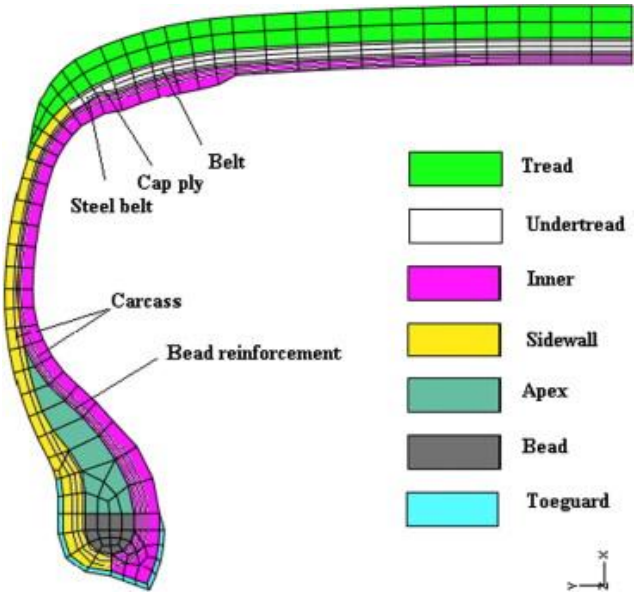

Figure 1.9 The generic composition of pneumatic tyres [25].

Pneumatic tyres for vehicles are generally made of a multi-layered composite structure primarily of rubber with various reinforcement sections as depicted in the Figure 1.9 [25].

Given that tyre composition is key to the overall strength of tyres, it is then important to understand the key areas where tyre deformation is most pronounced as well as the loading scenarios that are linked to these deformations. Ridha and Thieves have showcased just how significant the motion of a wheel is to the geometry of the tyre [26]. Ridha and Thieves placed a wheel free space to negate the effects of any vertical loading or slip and captured the geometry while it was both stationary and rotating, in the hopes of understanding how motion affects the sidewall shape of the tyre. They found that as the rotational velocity of a wheel increased, the upper sidewalls had a tendency to stretch away from the centre of the wheel. They believe this to be down to the centrifugal forces acting on the wheel as it rotates [26]. The stretching of the sidewalls they found is believed to be similar to what is experienced by a pneumatic tyre when it is inflated with increased levels of pressure. This created a potential new area of study, to determine whether the pressure within a tyre affects its overall deformation under operating conditions.

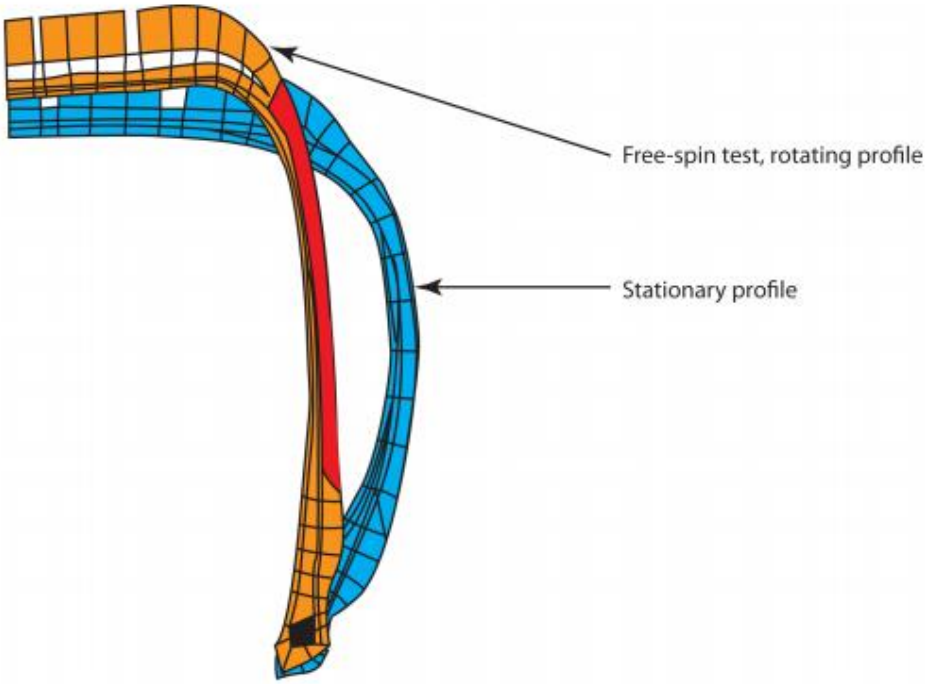

Figure 1.10: The findings of Ridha and Thieves [6, 26].

The findings of Ridha and Thieves are important when discussing tyre deformation on a loaded wheel given that the geometry of a rotating and stationary wheel showcase variance. Given that the tyre changes geometry so significantly, other setup parameters can be negatively influenced. If parameters such as the stiffness of the suspension system are not set up correctly, the tyre stretching could raise the axle height or create increased bulging at the contact patch; both of these situations can have negative impacts to the results of a wind tunnel experiment if not accounted for [6].

In order to understand how the rotation of a wheel affects the contact patch of a tyre, Sprot conducted a similar test to that of Ridha and Thieves however instead of the wheel spinning in the free air, he utilised a moving ground [6]. Sprot found that the tyre contact patch decreased in width by 3% which is significant given that the axle height was only raised by 1.5%. This proves that the contact patch is the area most prone to changes in operating parameters of a wheel. Sprot furthered his studies to understand how loading a tyre affects its overall deformation. A load was applied to a rotating tyre by changing the axle height by 9mm from 159mm to 150mm, 0.003 times the overall diameter of the wheel. Figure 1.11 showcases the cross-sectional deformation seen by a laser scanner.

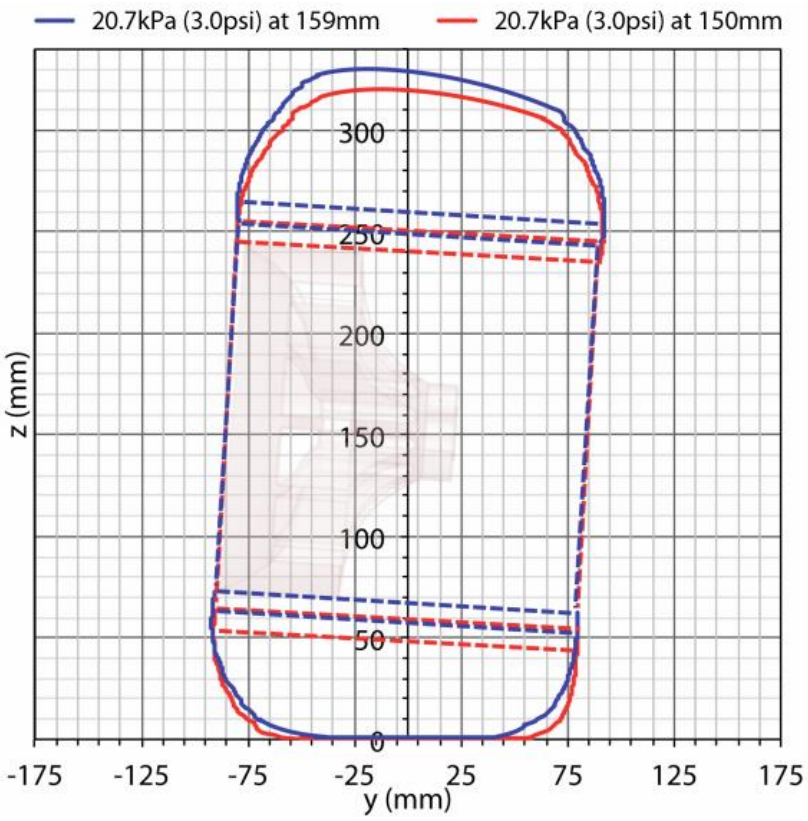

Figure 1.11: Rotating tyre profiles comparing loaded and unloaded conditions [6].

The wheel was set up with a camber angle between -3.2^{o} and -3.4^{o}, as a result, the majority of the deformation at the contact patch was seen on the inboard side of the wheel, due to the increased loading on this side of the tyre [6]. The outboard sidewall saw significantly less deformation however still experienced a small level of compression, this increased the overall area of the contact patch by 30%. However, this level of increase may be due to the camber angle, if the wheel was set up with 0^{o} camber, the increase in contact patch area would be expected to be less given that the concentrated load on the inboard side created such a large deformation spike [6]. By changing axle heights in steps, it was seen that the contact patch area would increase linearly, however, such results would not be expected in very high loading scenarios given the hyper-elastic nature of tyres [6].

Interestingly, the sidewall curvature over the top of the wheel between the two cases showcased small geometric differences that could potentially have significant aerodynamic consequences. The unloaded case sidewall appears to be more stretched and has a more angled top surface versus the loaded case. This suggests that in the loaded case, the sidewall did not recover completely from the compression experienced at the contact patch. This point is further proved by the fact that the overall diameter of the wheel decreased by 4% whereas the axle height was only decreased by 3% of the initial diameter, a 12mm decrease in diameter versus a 9mm drop in axle height [6]. This results in

the contact patch rotating about an axis that is approximately 10% lower than the rotational axis of the top of the wheel, suggesting that the wheel no longer retains its circular cross-section.

Increasing the pressure within the tyre had similar consequences on the curvature of the sidewalls that take place when a wheel rotates freely. The sidewalls stretch decreasing the size of the contact patch as well as increasing the overall diameter of the wheel. Interestingly, decreasing the tyre pressure made the contact patch more susceptible to changing loading parameters [6]. Changing the tyre pressure from 20.7kPa to 3.4kPa and conducting the same axle height test mentioned previously, the contact patch increased in area by 60% in the loaded scenario. This drastic change in tyre geometry due to inflation pressures showcases the large range of potential deformation scenarios that tyres will face under operating conditions.

1.2.2.2 Aerodynamics of Deformed Tyre Geometries

The vast majority of aerodynamic research has been conducted on rigid non-deformable wheels, as this takes away a series of parameters that make conducting simulations and experiments more difficult than deemed necessary. However, as will be discussed, the deformation of tyres can affect key flow structures associated with wheels. Currently, this field of research is relatively untapped, with very little to no information provided on isolated scenarios where tyre sidewalls are deformed [6].

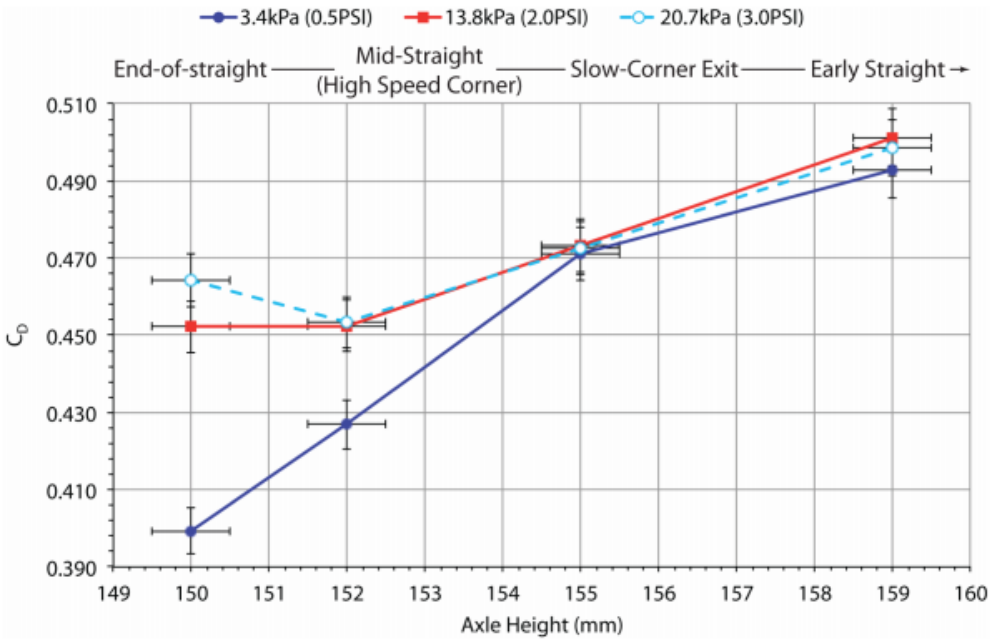

Figure 1.12: Wind tunnel drag data gathered by Sprot varying axle height and tyre pressure [6].

However, Sprot has provided aerodynamic analysis of a Formula One wind tunnel specified pneumatic tyre under load, with both experimental and computational data presented [6]. Although his study was not an isolated wheel study, it still provides information on how sidewall deformation affects the strength and direction of the two primary vortices and how this influences the flow structures elsewhere on the wheel.

Figure 1.12 showcases the drag coefficient data gathered from the wind tunnel test varying axle height and tyre pressures. Sprot found a noticeable decrease in drag coefficient when the axle height was lowered to provide the deformed geometry, with a 16% decrease between the 159mm and 150mm axle height. The overall frontal area reduction of the deformed tyre was only 2%, thus only accounting for 20% of the overall drag reduction. Interestingly, the increased deformation due to the change in axle height from 152mm to 150mm actually increased the drag coefficient. This is believed to be due to the sidewall folding over itself on the inboard side due to the high loading, this folding was not seen with lower tyre pressures, hence why this trend was not observed in the experiments with lower tyre pressure. Sprot was unable to provide any lift data, thus it is still unknown how these geometric changes affect this force value.

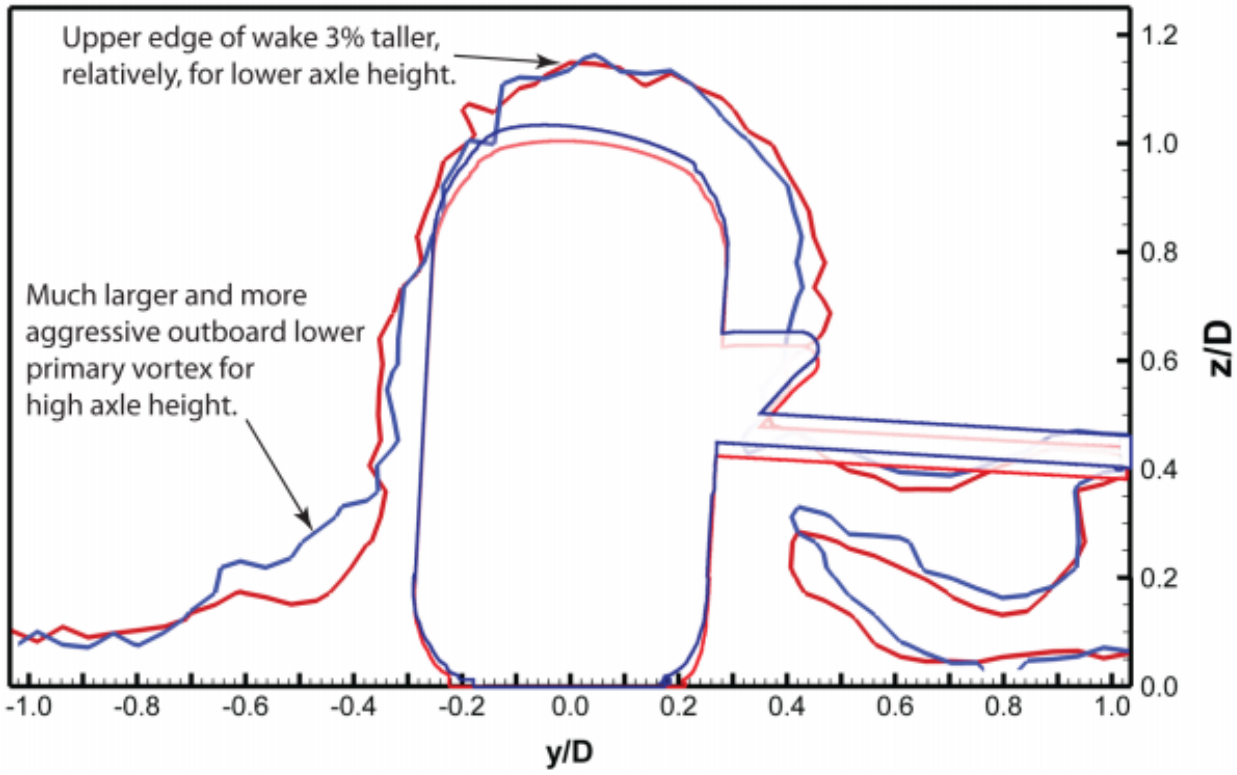

Figure 1.13: Outline of Cp = 0.9 at x/D = 1.5 or non-deformed (blue) and deformed (red) wheels.

There are significant differences in the flow structures associated with the different wheel geometries. Figure 1.13 showcases the outline of the wake structure of $C_p = 0.9$ at $x/D = 1.5$. It can be seen that the primary vortex on the outboard side is significantly lower and weaker compared to the non-deformed case. Due to the increase in the area underneath the sidewall of the non-deformed wheel, less energy is taken out of the flow before it reaches the contact. This and the fact that the ridge between the sidewall and tread is exposed causes this outboard vortex to have much more strength than its deformed counterpart.

The top surface of both geometries is relatively unchanged with the deformed geometry wake structure being 3% taller relative to its reduction in overall diameter. Given the intrusive method to mount the wheel in the wind tunnel, it is difficult to quantify the changes in the inboard primary vortex as the sting wake region is in such close proximity. Therefore, it remains relatively unknown how this sharp compression in the sidewall on the inboard side effects the strength and direction of the vortices in this region, showcasing the need to conduct isolated studies of deformed tyre geometries.

1.3 Project Aim and Outline

The main objective of this thesis is to showcase an understanding of how a tyre's shape is affected due to certain operating parameters such as rotation, inflation pressure and normal loading and how this geometrical change affects its aerodynamic performance. The deformed tyre geometry will be based on Fackrell's A2 wheel and will be created in CAD using knowledge gained from relevant literature.

The key aims of this study can be summarised as the following:

- Investigate the effect that centrifugal growth of tyres has on the aerodynamic performance of wheels.
- Investigate the effect that vertical loading on tyres has on the aerodynamic performance of wheels.
- Identify the areas in which the deformation of tyres most significantly affects the formation of key flow structures.

2 Computational Methodology

2.1 Background

CFD is a simulation tool that is governed by the laws of fluid mechanics. These being the conservation of momentum, conservation of mass and the conservation of energy. The Navier-Stokes equations are mathematical representations of this and are used by CFD to model fluid flow. These equations are momentum based time-dependent partial derivatives with no analytical solution that describe how the velocity, pressure, temperature and density of a moving fluid interact within closed two or three dimensional domains and as has been mentioned in the previous chapter, are often used to model the fluid flow around wheels [27] [28].

Previous studies on the flow structures associated with wheels suggest that the compressibility effects are largely negligible, only creating large-scale variance where the wheel is in interaction with other components such as diffusers [29]. Given that this study is of an isolated wheel and the Reynolds number of the simulation is lower, it can be assumed that the flow structures associated with the wheel will be incompressible in nature, thus there is no need to model the conservation of energy through the Navier-Stokes equations as there will be no accountable variation in density.

2.1.1 Governing equations of Fluid Flow

2.1.1.1 Conservation of Mass

The conservation of mass states that the change of mass of a fluid within a volume must remain constant [30]. For fluid flow, this is achieved by ensuring the mass flow rate of a system is equivalent to variations in overall mass. For 3D flow, this is presented as:

$$\frac{\partial \rho}{\partial t} + \nabla(\rho\vec{u}) = \frac{\partial \rho}{\partial t} + \frac{\partial(\rho u)}{\partial x} + \frac{\partial(\rho v)}{\partial y} + \frac{\partial(\rho w)}{\partial z} = 0$$

Where ρ is the density of the fluid and the u, v and w terms are velocity components of $\vec{u}$ in the Cartesian directions x, y and z. However, given that this investigation only considers incompressible flows, there will be no variation in density. Therefore the conservation of mass can be rewritten as:

$$\frac{\partial u}{\partial x} + \frac{\partial v}{\partial y} + \frac{\partial w}{\partial z} = 0$$

2.1.1.2 Conservation of Momentum

The conservation of momentum is based on Newton's second law of motion where the sum of the forces acting on a body is equal to the product of its mass and acceleration. For fluid flow, this law is applied to the variation of velocity as it passes through a domain, such that the sum of the forces is equivalent to the change in velocity. For incompressible flow, only the forces that act on the surface of a body effect the conservation of momentum [30].

The conservation of momentum of direction x and component u can be written as:

$$\frac{\partial(\rho u)}{\partial t} + \mathrm{div}(\rho u\vec{u}) = -\frac{\partial p}{\partial x} + \mathrm{div}(\mu\ \mathrm{grad}\ u)$$

By substituting the u and x terms with the corresponding terms with different directions, the three Navier-Stokes equations for momentum are derived.

2.1.2 Turbulence Modelling

The flow structures associated with wheels have been proven to be unsteady in nature [10]. This suggests that in order to accurately model such structures, unsteady solvers are required; this would require greater computational resources and time than what are available for this research project. However, it has been showcased that while the forces are not optimally obtained, the flow structures associated with wheels can be obtained accurately using a steady state solver, however no variance over time can be obtained [11, 10]. Given the limitations of resources available throughout this study, it has been determined that a steady state solver is best suited, as it has proven to be capable of modelling key flow structures associated with a wheel, these structures have been outlined to be the key area of investigation of this study.

Flow structures associated with objects can be characterised as either laminar or turbulent based on their Reynolds number, with increasing Reynolds number generating more turbulent flow [30]. For bluff bodies, the flow structures generated are generally of a turbulent nature. Given that a steady state solver will be used for this investigation, the Reynolds Averaging Navier-Stokes (RANS)

method is utilised to model these turbulent flow structures. The RANS method replaces the velocity and pressure terms in the original Navier-Stokes equations with a mean and fluctuating term [30].

$$u = \overline{U} + u' \qquad v = \overline{V} + v' \qquad w = \overline{W} + w' \qquad p = \overline{P} + p'$$

This allows the RANS method to account for turbulent regions by creating bounds in which new terms can be implemented. However, this ensemble averaging operation conducted on the Navier-Stokes equations creates six additional non-linear unknowns called the Reynolds stresses that require further computational modelling to be predicted [30]. Turbulence models are utilised to predict the Reynolds stresses, however, the method of predicting near and far wall turbulence varies, thus resulting in a range of turbulence models utilising different transport equations to solve for the transfer of momentum.

2.1.2.1 Realizable k-ε Turbulence Model

The realizable k-ε model was presented initially by Shih et al in 1995 [31]. It is based on the two equation, standard k- ε model, which resolves turbulent structures in the wake region of an object using the relationship between turbulent kinetic energy (k) and its dissipation rate (ε) [31]. The standard k-ε model, however, is known to have difficulty modelling near wall turbulence as well as swirling flows with high strain [30]. In order to resolve these issues, the realizable model modified the way both eddy viscosity and dissipation rate are calculated. The eddy viscosity term is calculated utilising a fluctuating term which is a function of the mean strain and rotation rate as opposed to a dimensionless constant utilised by the standard model [31]. These changes theoretically allow the realizable model to more accurately showcase near wall phenomena as well as and rotating flow structures.

Studies from McManus et al and Diasinos presented the improved effectiveness of the realizable model [3] [10]. Both studies were conducted using geometry utilised by Fackrell. They were able to demonstrate accurate prediction of the separation point over the top of the wheel as well as accurate representations of the flow structures generated from the contact patch, when compared to experimental data. In general, both computational studies demonstrated their superior ability at replicating the experimental results over alternative turbulence models available at the time. However, it has also been demonstrated that there is the need for near wall correction with this model and thus utilised the enhanced wall treatment method. In order to utilise this method, a non-

dimensionalised wall distance, y^+, of less than or equal to 1 is required to ensure accurate reproduction of flow structures forming from a surface [3] [32].

2.1.2.2 K-ω Shear Stress Transport Turbulence Model

Similar to the k-ε model, the k-ω model is also a two-equation turbulence that utilises the turbulent kinetic energy term. However, the k-ω model utilises the dissipation per unit of turbulent kinetic energy (ω) rather than the dissipation rate. The use of the ω term allows the turbulence model to more accurately define vortices associated with the flow [30]. It also does not require near wall correction that the k-ε models do [33].

The shear stress transport (SST) k-ω turbulence model was originally presented by Menter in 1994 [34]. In order to improve the effectiveness of the k-ω model in the freestream, the SST model transitions from the standard k-ω model on the inner layers of the boundary layer to a high Reynolds version of the k-ε model on the outer layers of the boundary layer as well as in the far field [34]. This allows the SST model to utilise the strengths of both the standard k-ω and k-ε models. Therefore with the SST model, characteristics of vortical structures can be obtained with greater accuracy as well as accurately predicted separation points without negatively influencing the generation of the wake region [34]. Therefore, this turbulence model should be ideal for predicting the separation of flow at the top of the wheel as well as accurately form vortices from the wheel surface.

2.1.2.3 K-kl-ω Turbulence Model

Unlike the k-ε and k-ω models mentioned previously, the k-kl-ω model is a three equation term that introduces a new term for the laminar kinetic energy (kl) [32]. The introduction of the kl term allows the model to predict the magnitude of low-frequency velocity fluctuations in the boundary layer, thus enabling it to better determine the point at which the fluid flow transitions from laminar to turbulent within the boundary layer [35]. In turbulent regions, the k-kl-ω model utilises the same infrastructure as the standard k-ω model, indicating that this model may not be able to depict the wake region accurately. Studies suggest that whilst this model does predict separation points accurately over an airfoil, it struggles to accurately model the reattachment of flow and further downstream flow structures [36]. Such reattachment of flow is not expected for wheels, however. Therefore, this

models improved modelling of the laminar to turbulent transition is desirable when looking at the separation point of flow.

2.1.2.4 Transition Shear Stress Transport Turbulence Model

The transition SST model is a four-equation turbulence model that expands on the ideas of the SST k-ω model [32]. Similar to the k-kl-ω model, the transition SST ideally targets to accurately capture the laminar to turbulent transition in the boundary layer. The method in which the transition SST model achieves this was initially presented by Menter et al in 2006 [37]. The model utilises two additional transport equations, one for intermittency and the other for transition onset momentum-thickness Reynolds number [32]. The intermittency deals with only local variables that influence the characteristics of the flow whereas the transition onset captures the non-local regions in correlation with the turbulent intensity that showcase a decay in turbulent kinetic energy. These two additional transport equations are coupled with the SST k-ω model, such that it is able to model the turbulent boundary layer and free stream regions with greater accuracy than the k-kl-ω model [32].

The Transition SST model has been showcased to model the separation point of an airfoil with equal if not better accuracy than the k-kl-ω model. However, it was able to model the reattachment of flow with greater accuracy when compared to experimental data [36]. The model also showcased the capability to model the wake formation with similar levels of accuracy to the SST k-ω and k-ε models, outlining the potential of the turbulence model to capture various intricate details of complicated flow structures. However, no studies have been performed on wheels utilising this turbulence model, therefore it is unknown how effective it will be at capturing flow structures associated with wheels.

2.2 Numerical Methods

The software package utilised for both the meshing and the solving of this investigation was ANSYS Fluent 17.2. ANSYS Fluent is frequently used in academia and is a commercially available software package commonly used for aerodynamics research and industry [6]. ANSYS utilises the finite volume method as its finite difference scheme to calculate the motion of fluid flow within a set domain. The finite volume method requires the fluid domain to be created by a discrete number of cells [28].

2.2.1 Finite Volume Method

This method divides a volume of a known quantity in control volumes generally referred as elements or cells. The shape of these elements is determined by the meshing technique specified, these could be tetrahedral, hexahedral or polyhedral, with each method having their own advantages and disadvantages. Each of these elements are then used to calculate the fluid flow through a domain, thus the quality, the skewness and aspect ratio, of these elements is paramount to ensuring accurate results [30]. In order to capture flow structures that generate large pressure or velocity variations, an increased meshing resolution is required to accurately resolve these regions. The location of these structures must be identified before the meshing process.

2.2.2 Discretization Technique

In order for CFD to solve for fluid flow, the governing equations must be in a discretised form. This process converts the governing equations into a series of algebraic equations that are solved at the centre of each element, ensuring that any information gained can be passed to adjacent cell centres [30]. In order to achieve this, Fluent provides a number of upwind discretization schemes [32]. Upwinding discretization schemes provide more transportiveness than central differencing schemes as well as accounting for the direction of flow, meaning they calculate cell values from up to downstream. However, the upwind schemes do diffuse the flow more than central differencing methods, but the improved transportiveness makes the scheme more desirable for this study [30].

To reduce the diffusivity present in the upwinding schemes, Fluent provides the second-order method. With first-order upwind schemes, the solver assumes that the values at the centre of the cell are equal to those at the face [32]. Whilst this provides a more efficient and stable solution, the high amounts of diffusion can lead to less detail in the structures formed. The second-order scheme utilises a Taylor series expansion of the cell centre value to compute the face values of that same cell. This leads to more accurate solutions, however, can lead to instabilities in the solver; thus requiring a higher quality mesh to solve [32]. Due to the overall stability of the simulations and given the need for the accurate recreation of the flow structures associated with wheels, it was decided that a second-order upwind scheme should be used.

2.2.3 Solution Process

Given the incompressible nature of this simulation, a pressure based solver will be utilised [38]. Fluent offers two methods to solve the governing equations, either in a coupled or segregated manner. The segregated method solves the u, v, w and p terms individually, thus only one equation is needed to be discretised at any given moment. This allows the solver to utilise less memory however it can take longer to reach a converged solution.

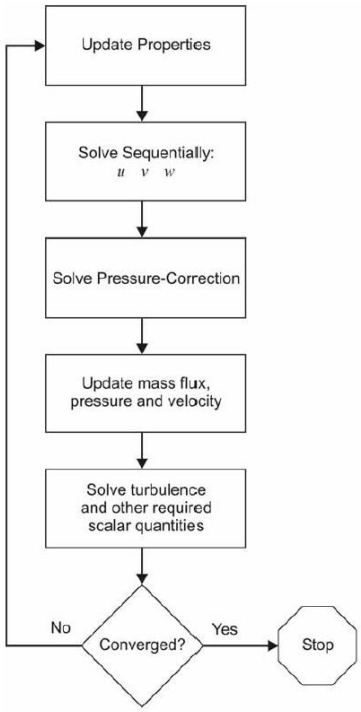

Figure 2.1: Flowchart showcasing the segregated pressure based solver [3].

Figure 2.1 depicts the process the segregated solver uses to reach a converged solution. The velocity components are calculated before the solver attempts to calculate pressure. The solver then attempts to correct these values through a velocity-pressure coupling, followed by a re-calculation of the turbulence properties [32]. To improve the stability and efficiency of this system, Fluent utilises the semi-implicit method for pressure linked equations (SIMPLE). The use of this implicit technique allows the solver to store the data from the iteration to calculate the variables for the current iteration. To further improve the stability and rate of convergence, the SIMPLE-Consistent or SIMPLEC can be utilised. The SIMPLEC model changes the method of correction for the face flux values, improving the overall convergence of the solver at a cost of computational time.

The coupled method solves the velocity and pressure equations simultaneously by coupling the pressure based continuity equations and the conservation of momentum equations. This method requires 1.5 to 2 times more RAM than the SIMPLEC method [32]. However, solving velocity and pressure simultaneously decreases the number of iterations required to reach a converged solution. Given the RAM quantity in the machines that were primarily used, this method was not able to be utilised and thus the SIMPLEC method was used to ensure an accurate converged solution could be reached.

2.2.4 Convergence Criterion

With simulations on wheels, it is expected that force fluctuations, lift and drag, will exist given the unsteady nature of the flow. This is compounded by the fact that with these simulations, the force fluctuations would increase as the mesh became denser. As such, it was deemed that once the force fluctuations became oscillatory in nature, with the variance after every 500 iterations being less than 3% relative to each other, and the scaled residuals reached values less than 10^{-4}, a converged solution was achieved. The scaled residuals vary for different turbulence models due to the differing transport equation, however, continuity, x, y and z velocities remain consistent throughout. To reach these values, 8000 iterations were required after initialising the flow with the inlet parameters. Ideally, more iterations would converge the solution further, however, given time constraints, this was not achievable nor deemed necessary.

2.3 Model Description

2.3.1 CAD Model Description

The wheel geometry was modelled using 3D CAD software CREO Parametric 4.0 and was based on Fackrell's A2 wheel given the concerns regarding the force measurements of the B2 wheel. The wheel had a diameter of 416mm and a width of 191mm. The rim profile was slight asymmetric in nature with the side with the deeper section taking as the inboard side of the wheel. The contact patch was created using the methods utilised by Diasinos [3]. However, further study in this area was conducted and a height of 0.002D was chosen rather than Diasinos' 0.0028D due to an improvement in results.

The 0.002D step height achieved values that were 6% and 3% closer to Fackrell's experimental data for drag and lift respectively when compared to the step height of 0.0028D Figure 2.2 showcases the contact patch design and dimensions of the A2 wheel.

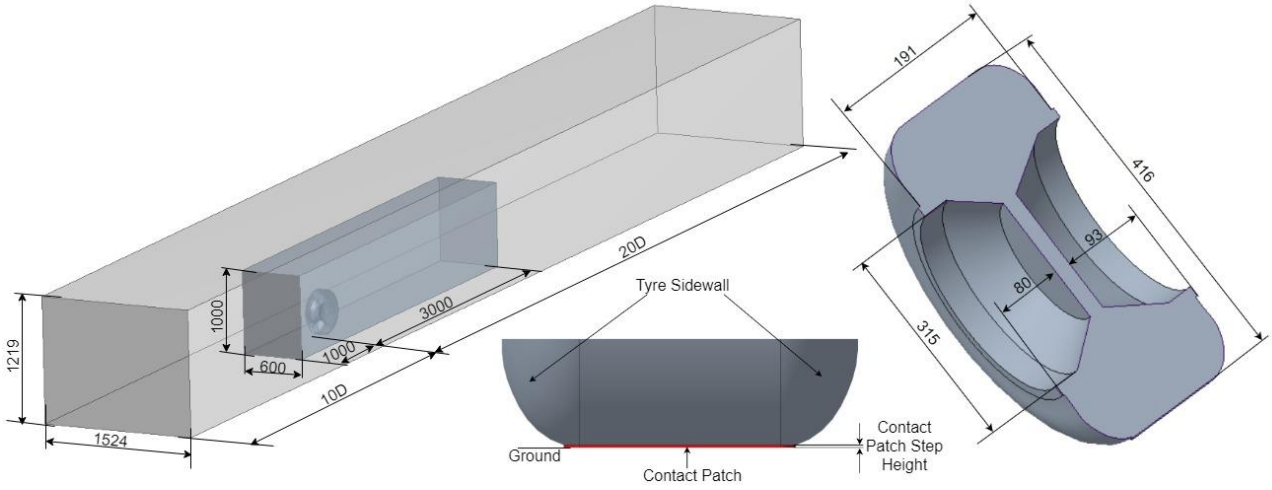

Figure 2.2: Contact patch design used for CFD simulations and wheel and domain sizing. All dimensions to the nearest mm

The width and height of the domain were 1524mm by 1219mm in order to match the sizing of Fackrell's wind tunnel [7]. To ensure that the inlet and outlet boundaries did not interfere with the solution of the simulation, the inlet was positioned 10D in front of the wheel and the outlet was 20D behind the wheel as it was assumed that this was a sufficient distance away. Boundary convergence checks presented in section 3.1 confirmed that these dimensions were suitable.

2.3.2 Meshing Process

For the meshing process, ANSYS Mechanical was utilised to create a tetrahedral mesh around the wheel geometry. Given the need to test multiple different geometries and the time frame in which this investigation needs to be completed in, a structured mesh was not considered. The tetrahedral mesh allows for cells to be concentrated around areas where important flow structures are generated from such as the contact patch. To further aid with this, as well as improve the mapping of the wake region, a body of influence was created. The body of influence was 0.6m wide to capture the full width of the wake, 1m high to accurately capture the separation point, 1m in front of the centre of the wheel to reduce the effects of rapid size reduction in the mesh and 3m behind the wheel to capture the full length of the wake.

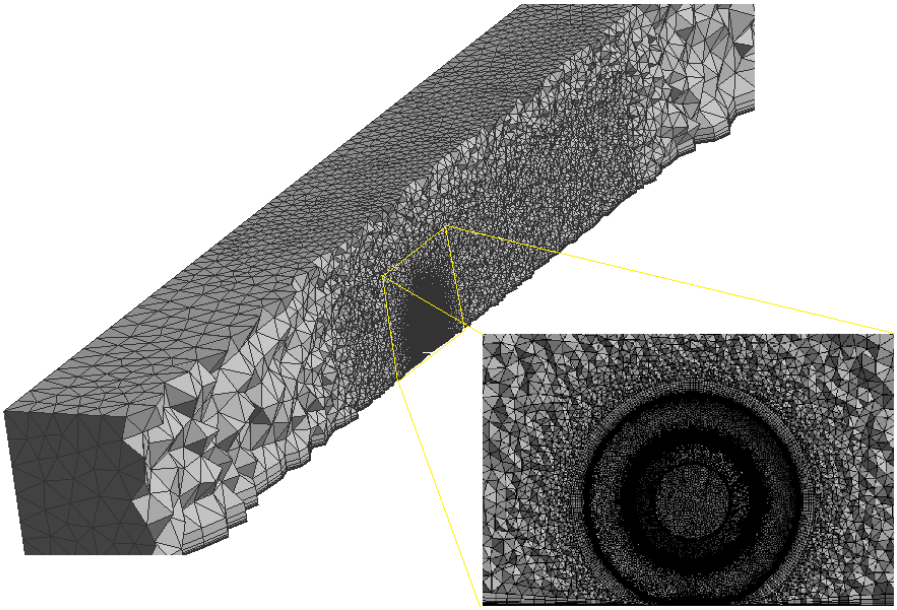

Figure 2.3: The interior mesh showcasing the body and face sizing around the wheel geometry as wheel as the inflation layers.

To ensure that the C_P pressure peak seen in Fackrell's experiment was captured in this investigation, the mesh surrounding the contact patch was made denser than surrounding areas. Therefore, the mesh on the face of the contact patch was generated ensuring at least 20 elements were created across that gap. The mesh grew out from this face with a growth rate of 1.05 whilst still ensuring the minimum number of elements across any given gap was 5. This procedure allowed the C_P at the face of the contact patch to be similar to what was seen in Fackrell's experiment. The sizing on the wheel itself was set to a max size of 5mm with the body of influence set to 40mm. The global max size was set to 200mm to reduce the overall number of elements in the mesh. The global growth rate was set to 1.1 to avoid the risk of rapid expansion in the size of elements.

As mentioned previously, to ensure the accuracy of this simulation, a y^+ of less than or equal to 1 is required. To ensure that this is the case, the first layer thickness of the inflation layer can be calculated for the flow over a plate using the formula:

$$y^+ = \frac{\rho u_r y_p}{\mu}$$

Where ρ is the density of the fluid, μ is the kinematic viscosity, u_r is the friction velocity and y_p is the distance from the boundary to the centre of the first cell in the inflation layer. However, given that this investigation is not for plate flow, this value can only be used as a reference. Therefore, it needs to be checked ensuring that the y^+ is less than or equal to 1. Using this method with a Reynolds number of 5.3×10^5, matching Fackrell's experiment, it was determined that a first layer thickness required for both the wheel and ground was 0.01mm when and as such was set to this value [7]. To ensure that

the entire boundary layer of the wheel is captured by the mesh, a similar technique can be used to create an initial starting value.

$$\delta = \frac{0.37l}{Re_l^{1/5}}$$

Using the formula above, the boundary layer thickness (δ) for plate flow can be calculated of a length (l). Using the first layer thickness approach, it was determined that 35 layers are required in the inflation layer with a growth rate of 1.2. This growth rate was selected to ensure a good aspect ratio between each layer in the inflation layer. For the ground, a last aspect ratio method was used as the cells near the ground change in size drastically throughout the domain. 15 layers were used in the ground with a last aspect ratio of 0.3. These parameters were checked and verified to be appropriate. The total number of elements in this mesh was approximately 15 million.

2.3.3 Boundary Conditions

The following boundary conditions were set and kept constant for all simulations, unless specified otherwise:

- Inlet was set with a constant velocity of 18.6 m/s.
- The outlet as a constant pressure outlet with 0 Pa gauge pressure.
- Turbulent intensity and length scale of 2.9% and 0.02912m was used for both the inlet and outlet to match Fackrell's experiment [7].
- Far Field Walls were set with symmetry conditions so that the flow showcases no variation along the symmetry direction. This negates the need to create inflation layers on these walls as no boundary layer will be formed.
- The ground was set as a moving ground with a translation velocity of 18.6 m/s in the same direction and the freestream velocity. This allows for the correct formulation of the boundary layer on the ground as the flow moves downstream.
- The wheel was set as a no-slip rotating wall with a rotational velocity of 89.43 rad/s matching the tangential velocity of the wheel tread to the freestream and ground velocities. This velocity was increased and decreased when the diameter of the wheel was changed.

3 Validation and Verification

To showcase the accuracy of a computational model, the American Institute of Aeronautics and Astronautics (AIAA) defines two methods [39]:

- Verification: “The process of determining that a model implementation accurately represents the developer’s conceptual description of the model and the solution to the model”.
- Validation: “The process of determining the degree to which a model is an accurate representation of the real world from the perspective of the intended uses of the model”.

Whilst it is not necessary, it is recommended that the validation process occurs once the model is verified. It is important to note that the validation process does not require an accurate agreement between the two results but rather showcase accurate representation of trends [39].

3.1 Verification

3.1.1 Grid Convergence Study

A grid convergence study was conducted on Fackrell’s standard A2 wheel with the boundary dimensions mentioned in chapter 2. An initial coarse mesh with 11 million elements was created and run to generate baseline values for lift and drag. This mesh was refined with approximately 2 million element increments each with a total of three refinement stages. Thus resulting in approximately 13, 15 and 17 million element meshes being run. Given the restrictions due to computational hardware, meshes greater than 17 million were not able to be run. The lift and drag coefficient variations between each run have been presented below, with the variance being presented relative to the finest mesh utilised.

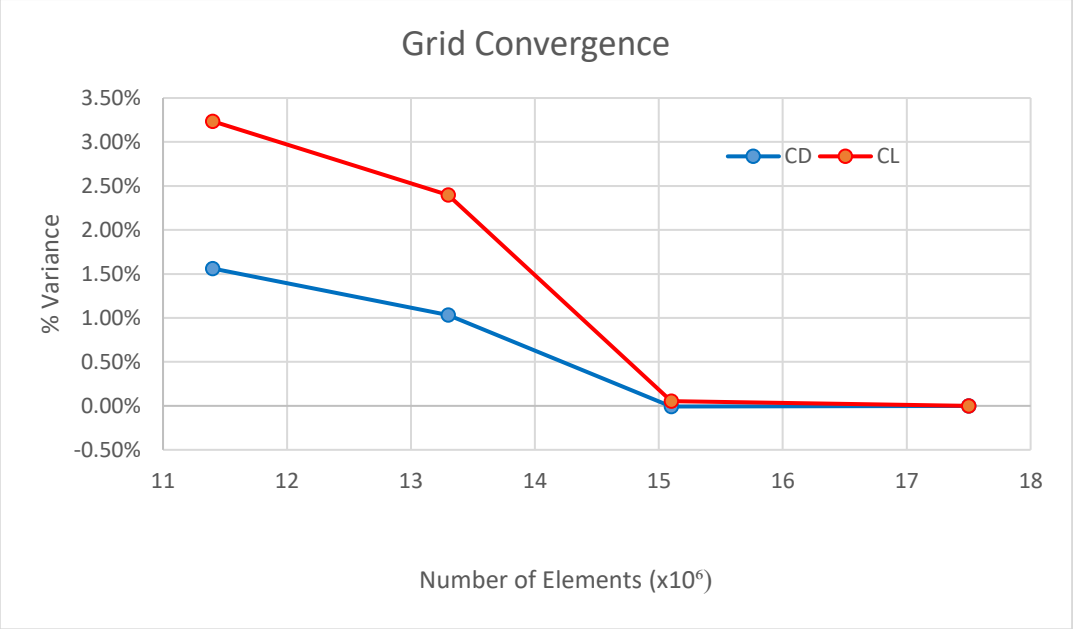

Figure 3.1: Lift and drag coefficient variance with different mesh density.

From the graph above, it can be seen that there was no variance above 4% for any of the meshes tested relative to the finest. However, the results suggest that the lift and drag will not alter by more than 0.25% for meshes with more than 15 million elements.

In order to expand the understanding of the errors associated with the lift and drag of the wheel due to the varying mesh density, the Grid Convergence Index (GCI) is utilised. The GCI utilises the Richardson extrapolation technique and is used to calculate the error associated with a specific parameter at a specified mesh density in relation to a theoretical asymptotic value [40]. The errors are calculated using the following formulas:

$$E_1 = \frac{\varepsilon}{r^p - 1} \quad E_2 = \frac{r^p \varepsilon}{r^p - 1}, \varepsilon = \frac{f_2 - f_1}{f_2}, r = \frac{h_2}{h_1}$$

Where p is the order of convergence being used, f is the parameter specified, h is the number of elements and 1 and 2 correspond to coarser and finer grids respectively. The error calculations are used to calculate GCI using the formula below, where F_s is the factor of safety:

$$GCI_1 = F_s|E_1| \qquad GCI_1 = F_s|E_2|$$

Given that the 15 million element mesh showcased the lowest variance and the other meshes experienced high errors, it is the only grid being considered for the GCI calculation using the 17 as the base. Given that only two grids are being used, the F_s is 3 [40]. Given that second order convergence is used, the value for p is 2. The GCI calculations are presented in the table below.

Table 3.1: Grid convergence index for coefficients of lift and drag.

	GCI (15m Elements)	GCI (17m Elements)
CD	0.09%	0.06%
CL	0.65%	0.48%

As can be seen from the table above, the 15 million element mesh only varies in results by a maximum of 0.17%. This was deemed acceptable and thus the 15 million element mesh was deemed more suitable for future studies due to its improved computational time without damaging the accuracy of the results.

3.1.2 Boundary Position Study

Given that the top and sidewall positions of this study were designed to match the wind tunnel used in Fackrell's experiment [7], only the inlet and outlet positioned were varied. The inlet was initially placed at 10D in front of the centre axis of the wheel and the outlet was set to 20D behind. By increasing these distances in 2D increments, it can be determined whether the positioning of the inlet and outlet has any influence on the accuracy of the results. To ensure consistency, for the inlet distance checks, the outlet positioned remained at 20D and for the outlet checks, the inlet remained at 10D. Increasing the position did not affect the size of the mesh greatly, due to the meshing strategy, therefore it was deemed unnecessary to test closer positions.

The variance due to the inlet position was less than 0.5% for the coefficient of lift and 0.23% for the coefficient of drag. For outlet position, these numbers were -0.08% and 0.08% respectively. Given these results were smaller than the variance presented by the GCI calculations, it was decided that the original boundary positions of 10D to the inlet and 20D to the outlet were to be utilised.

3.2 Validation

3.2.1 Lift and Drag Comparison

The C_D and C_L values of Fackrell's experimental studies are presented in Figure 3.2. The turbulence models mentioned in chapter 2 were all assessed in comparison to Fackrell's results to determine

which is best suited for this study. The C_D and C_L values are in reference to the frontal area of the wheel which is 0.0795m^2.

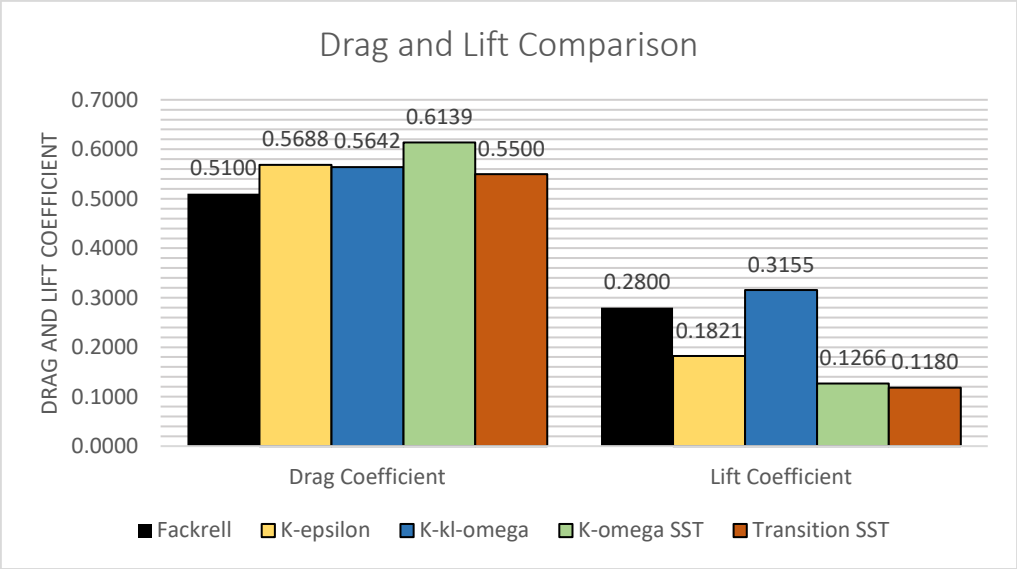

Figure 3.2: Drag and lift comparison of Fackrell's A2 wheel with CFD.

From Figure 3.2, it can be seen that all turbulence models over-predicted drag and, with the exception of the k-kl-ω model, under-predicted lift. In general, the k-kl-ω correlated best with Fackrell's data. However, as will be discussed in the following chapter, the k-kl-ω model did not resolve the trends associated with wheels as well as the other turbulence models. Under-prediction of lift in CFD simulations of wheels is expected as Fackrell mentioned the fact that 30% of the lift generated by a wheel is generated in the contact patch region [7]. This region is not able to be computed due to the simplifications made to the contact patch geometry, as showcased in chapter 2. Another area that may be affecting correlation of results is the fact that this was a steady state simulation. It has been well documented that for rotating wheels, unsteady simulations are required for higher accuracy [10]. Taking this into account, it is interesting that the k-kl-ω model over-predicts this value. The k-ε turbulence model predicts the lift and drag of the A2 better than both the SST models. This is the expected result due to the ability of this turbulence model to resolve the flow in the boundary layer as well as the wake region [32].

3.2.2 Pressure Distribution

As mentioned previously, in order to validate a CFD simulation, it must showcase accurate recreation of trends associated with the flow structures that stem from the object. One such method to determine

this for a wheel is through the coefficient of static pressure distributions on the surface along the centreline; this can also be taken further by showcasing this distribution at other locations. The coefficient of pressure plots for the various turbulence models is plotted against Fackrell's experimental data below.

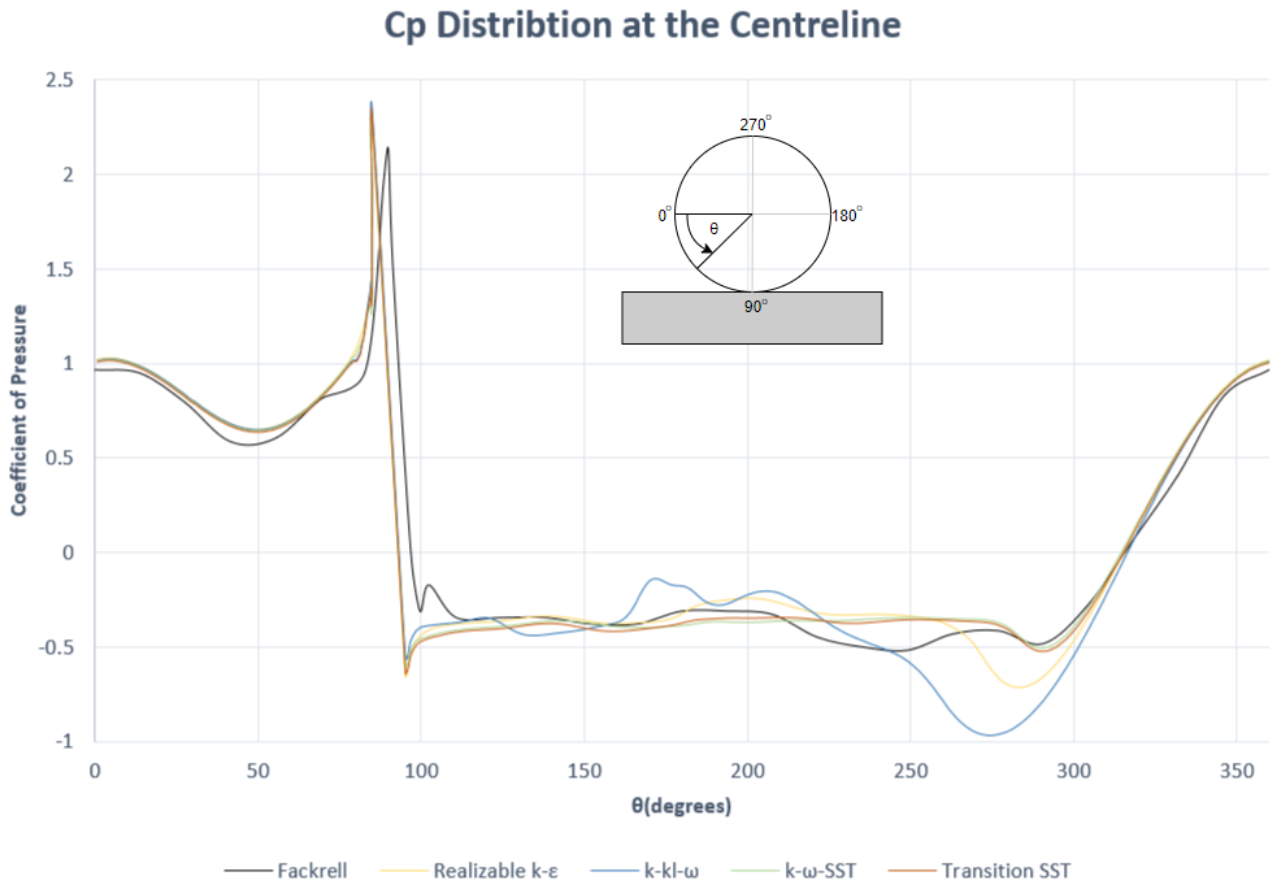

Figure 3.3: Coefficient of static pressure at the centreline of the A2 wheel with varying turbulence models.

From Figure 3.3, it can be seen that the CFD results do align with Fackrell's experiment well, with the exception of the k-kl-ω model. Looking at the region between 70 and 100 degrees, it can be seen that all turbulence model replicate the positive pressure peak as well as the negative peak seen by Mears [8]. Given the similarities between the turbulence model and the results of previous simulations, it has been concluded that the capture of this region is more dependent on the density of the mesh at the contact patch than the turbulence model. The trends also suggest that if the geometry had not been manipulated, both the positive and negative pressure peaks would be greater than depicted here.

The discrepancies between each turbulence model and Fackrell's data is primarily in the region behind the wheel to the separation point above it (approximately 100-270 degrees). At this region, the two primary vortices are expected to be the dominant flow structures present. This is where the

difference in the method of which the turbulence models calculate turbulence has the greatest effect. It can clearly be seen that the k-kl-ω model struggles greatly within this region, whereas the two SST and k-ε models predict the formation of these structures with increased accuracy.

The k-kl-ω model also showcased poor correlation at the separation point over the wheel (250-290 degrees). This result aligns with literature that mentioned this turbulence models' poor ability at replicating the regions beyond the separation point of an airfoil [36]. However, as predicted by literature, the Transition SST and k-ω SST models predict and model this separation point well, showcasing how the addition of the SST code improves the standard k-ω code. The k-ε model captured the separation point with similar accuracy to the two SST models however showcased a greater negative peak. This again aligns with literature, as this negative peak is the result of the formation of vortices due to the separation of flow, therefore it is expected that the SST models perform better in this area.

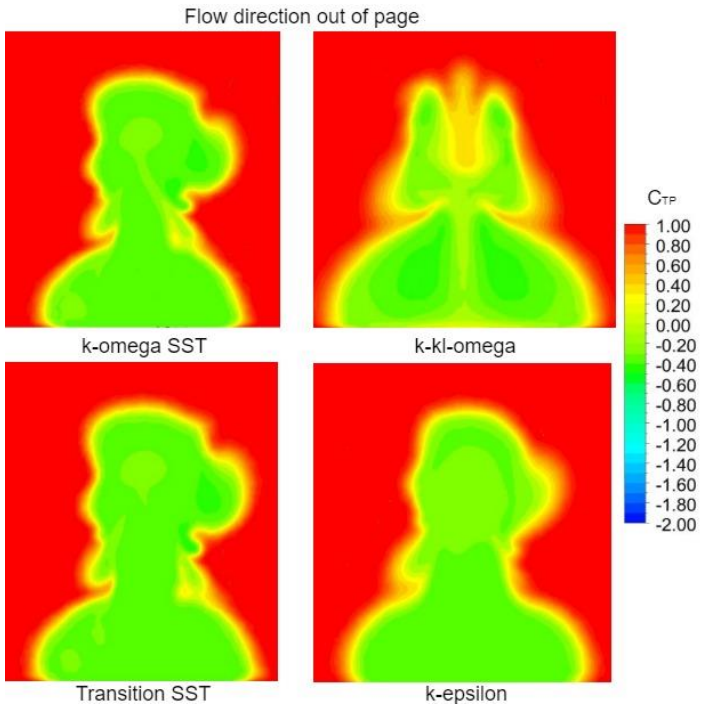

Figure 3.4: Coefficient of total pressure at x/D = 0.52 for the turbulence models tested.

As it can be seen from Figure 3.4, the k-kl-ω struggles to model the wake structure of the wheel. However, the other three turbulence models all present similar structures and are able to identify the same flow structures. Given these finding and the fact that the k-ε model was able to predict the forces better, it was determined that this turbulence model was most suitable for further studies.

4 Results and Discussion

4.1 Geometric Changes of the A2 Wheel

A total of 5 cases of differing geometries were tested. These cases were designed to replicate the deformation expected from normal operating conditions of wheels. These conditions were the centrifugal growth due to rotation or increased tyre inflation pressure, the increased vertical loading due to braking as well as the compression of the sidewalls due to a decrease in tyre inflation pressure presented [26] [23]. Both of these cases had two steps, a standard step and the maximum step.

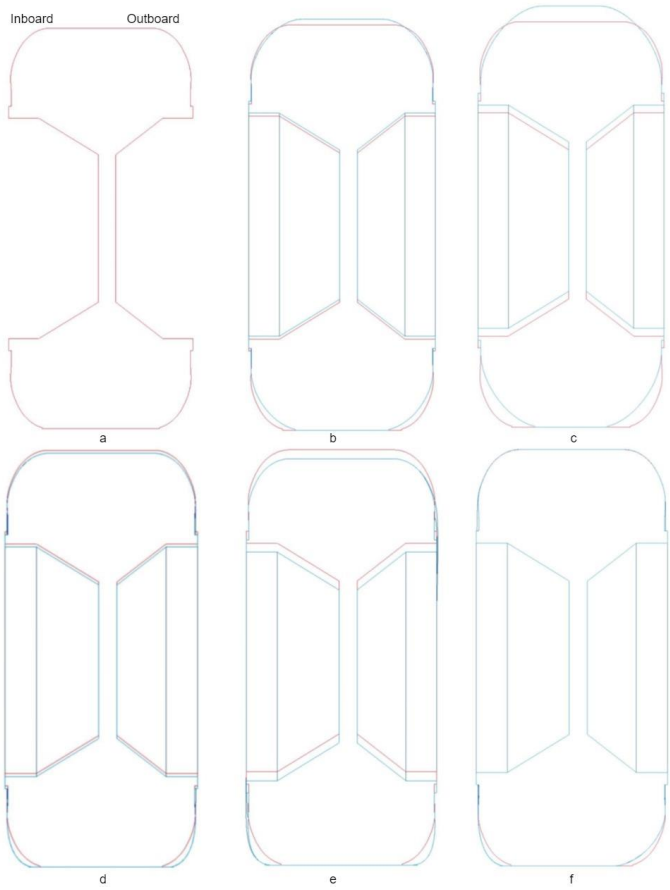

Figure 4.1: The geometries tested (blue) compared to Fackrell A2 wheel (red) - (a) Standard A2 wheel (b) Centrifugal growth 1 (CG1) (c) Centrifugal growth 2 (CG2) (d) Vertical loading 1 (VL1) (e) Vertical loading 2 (VL2) (f) Asymmetric case (AS1)

A fifth case was created after drawing inspiration from the findings of Sprot [6]. This case presented an asymmetric deformation of the sidewalls due to normal loading on a tyre with a camber and slip angle. This case had increased vertical loading on the inboard side of the wheel and centrifugal growth on the outboard side. A section view of each of the cases at the wheel centre is showcased in Figure

4.1. The standard Fackrell A2 wheel has also been displayed to showcase the magnitude of the changes. More detailed images of each wheel are presented in Appendix A.

Each case was created with the ideal gas law in mind, the fact that if there is no change in density or temperature, the volume should remain constant. Thus, the total volume of each tyre in the region where the air is present showcase variances of less than 1% off of Fackrell's A2 wheel. In order to achieve this, the overall diameters of the CG1, CG2, VL1 and VL2 wheels have changed, as seen in Figure 4.1. The AS1 wheel, however, did not require a change in diameter. The CG1 wheel had an increase in diameter of 5mm, 16mm increase for the CG2 wheel, a decrease of 5mm for the VL1 wheel and a 9mm decrease for the VL2 wheel.

As discussed in chapter 2, the contact patch shape has large impacts on the formation of the two primary vortices. The general shape of the contact patch does not vary greatly between each case, however, the width showcased large variations. It was seen that as the sidewalls grew centrifugally, the contact patch width is decreased. The opposite is the case for when the vertical loading is increased. Similar changes in the length are also seen, resulting in the centrifugal growth cases having smaller contact areas than the increased vertical loading cases. For the VL2 wheel, the contact patch shape is more oval in nature, this is due to the extreme loading on the wheel, see Appendix A. The AS1 case's contact patch is off the centre axis of the wheel, due to the asymmetric deformation. The contact patch shapes for each wheel have been presented in Appendix A.

4.2 The Effect of Centrifugal Growth

4.2.1 Lift and Drag Comparison

It was seen that the magnitude of the geometric change had effects on the lift and drag of the wheel. The table below showcases the lift and drag coefficient values of each case simulated.

Table 4.1: Lift and drag comparison of the centrifugal growth cases.

Wheel	Drag Coefficient	Lift Coefficient	% Variance Drag	% Variance Lift
A2	0.5688	0.1821	N/A	N/A
CG1	0.5504	0.1611	3.23%	11.53%
CG2	0.5108	0.1351	10.20%	25.83%

Looking at the two centrifugal growth cases, there is a visible trend that showcases a general decrease in drag and lift as the centrifugal growth of the sidewalls is increased. It is also evident that the deformation of the sidewall affect the lift more than it does the drag. Further discussions showcasing why this is the case is presented is the following sections.

4.2.2 Pressure Distribution Comparison on the Wheel Surface

Given the large variations in the force values seen on the differing wheel geometries, it is important to generate an understanding of why this is the case. Static pressure distribution on the surface of the wheel can give a good indication of the force acting on the wheel. Figure 4.2 showcases the coefficient of static pressure on the surface of each wheel at the centreline.

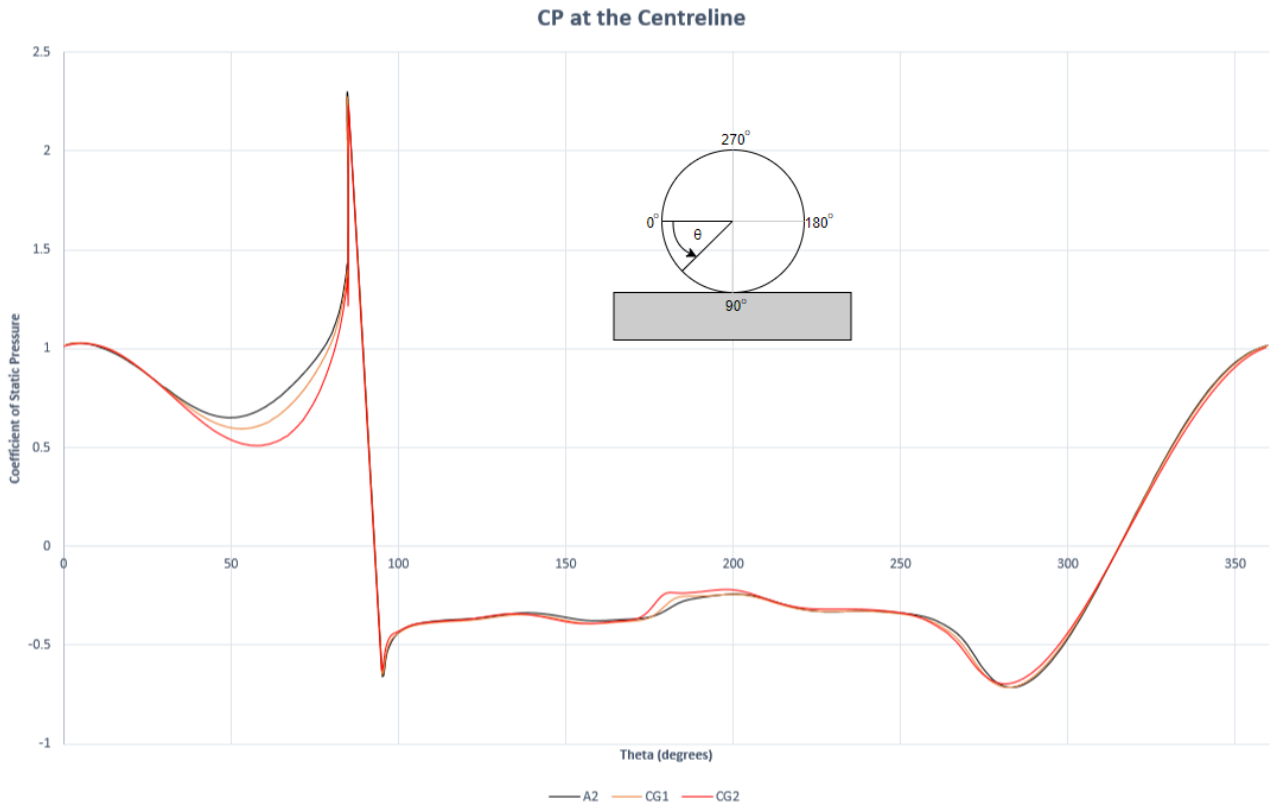

Figure 4.2: Coefficient of pressure distribution around the centreline of the centrifugal growth cases.

Initially looking at the region between 30 and 70 degrees, it can be seen that the CG1 and CG2 wheels experience a greater pressure drop compared to the A2 wheel. This is due to the velocity of the air that travels to the underside of the wheel. With the growth of the sidewalls in the CG1 and CG2 wheels, the increase in the area underneath the wheel promotes an increase in the air to flow in this region, resulting in the lower and later pressure troughs seen in Figure 4.2, approximately 60 degree

for CG1 and 70 degrees for CG2. This should also affect the positive pressure peaks seen at the front of the contact patch. However, both the CG1 and CG2 wheels did not see an increase in this peak value, instead, a decrease in peak value was observed. This paired with the fact that the flow has less distance to cover to reach the outer edges of the contact patch suggests that the increase in flow rate was more influenced to travel around the contact patch towards the straighter sidewalls, thus explaining the decrease in lift and drag generated by the wheel. The deformed sidewall shape did not affect the separation point, with the minor variations being primarily down to the increase in diameter of each wheel.

4.2.3 Flow Field Observations

In order to generate an understanding of the flow structures surrounding the contact patch, coefficient of total pressure plots are created at half the height of the of the step size of the contact patch. These plots are shown for each tyre geometry tested in Figure 4.3.

Large variations in the generation of the two main vortices can be seen in each case. It can be seen in the CG1 and CG2 wheels that the formation of these vortices is delayed, causing a narrower wake structure to be formed. This also seems to suggest that the energy contained in these vortices is greater, leading them to be larger in size and be carried further downstream.

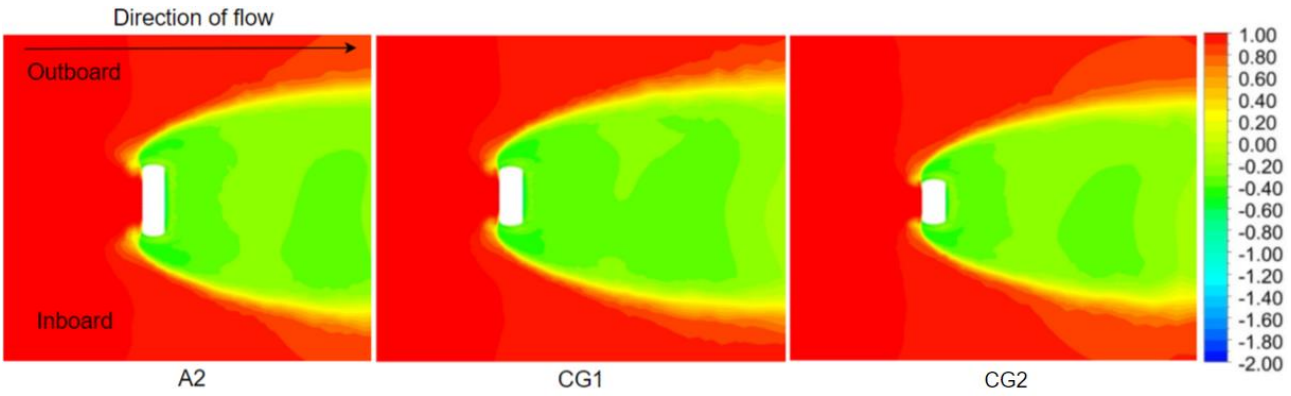

Figure 4.3: Variations in the wake structure due to centrifugal growth at z=0.01D

To further understand how these flow features affect the wake structure further downstream, total pressure plots can again be created, this time normal to the flow. Figure 4.4 depicts this such that x/D = 0.52. Vectors have been plotted tangential to the surface to showcase the direction of the velocity in a given region.

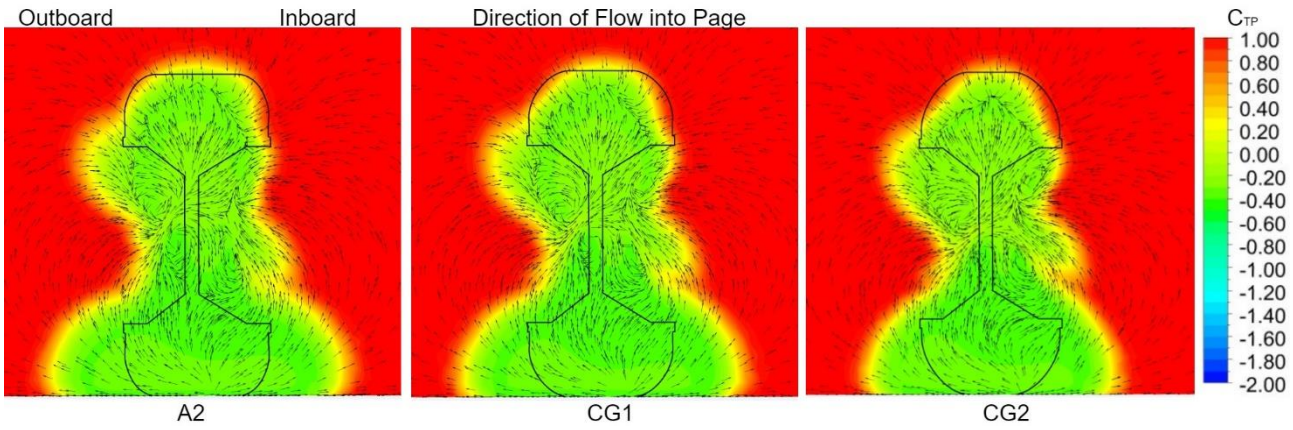

Figure 4.4: Variations in the wake structure due to centrifugal growth at x/D = 0.52.

As can be seen from Figure 4.4, the variation in the wake structure immediately behind each wheel is minimal. However, the stretched sidewalls of the CG1 and CG2 wheels leading to a narrower wake at the top. Given that the separation point over the top of the wheel is similar across all wheels, there was no real height change in the wake. The areas that saw the most significant changes were the locations of the two primary vortices. The more energetic vortices that were formed from the CG1 and CG2 wheels resulted in a taller wake. The wake was also narrower, but this is potentially due to the narrower contact patch of these wheels.

Travelling further downstream to x/D = 1.2, the effects of the sidewall deformation is more pronounced, showcasing not only variations in the energy of the flow but also significant variations in the wake structure. In order to showcase the energy variations in more detail, the scale for the plot was changed. The total pressure plots are presented in Figure 4.5.

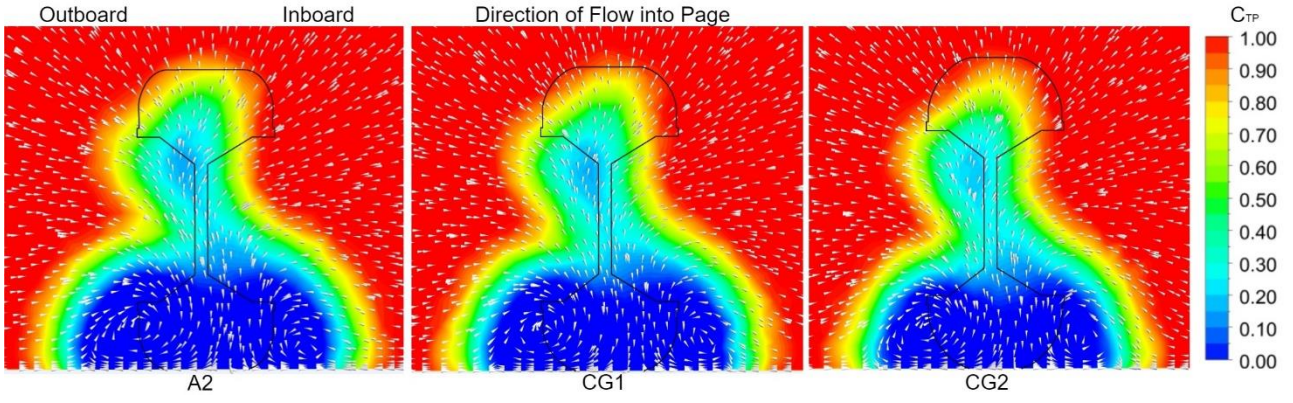

Figure 4.5: Variations in the wake structure due to centrifugal growth at x/D = 1.2.

It can immediately be seen that the increase in energy present in the two main vortices of the CG1 and CG2 wheels has resulted in these vortices carrying more strength downstream, showcased by the increase in rotational velocity in Figure 4.5. The height of the wake relative to the diameter of the

wheel also saw variations. Due to the interactions with the two primary jetting vortices, it can be seen that the height of the wake reduced in the CG1 and CG2 wheels.

4.3 The Effect of Increased Vertical Loading

4.3.1 Lift and Drag Comparison

Unlike the centrifugal growth cases, the increased vertical loading cases did not showcase a trend in regards to the lift and drag coefficient. This can be seen in the table below.

Table 4.2: Lift and drag comparison of the increased vertical loading cases.

Wheel	Drag Coefficient	Lift Coefficient	% Variance Drag	% Variance Lift
A2	0.5688	0.1821	N/A	N/A
VL1	0.5707	0.2076	-0.33%	-14.02%
VL2	0.4670	0.1577	17.89%	13.39%

It can immediately be seen that both the drag and lift increased for the VL1 wheel, whereas the opposite occurred for the VL2 wheel. However, the drag increase for the VL1 wheel is negligible as the variance was within the error calculated by the GCI. Interestingly, the VL2 wheel saw greater force fluctuations, in comparison to the other wheels tested, when the solution was calculating. The VL1 wheel force variance was approximately 5% whereas the VL2 wheel varied by approximately 10%. This may potentially skew results. However, as will be discussed, the VL2 wheel showcased vastly different flow structures compared to the other wheels.

4.3.2 Pressure Distribution Comparison on the Wheel Surface

The coefficient of static pressure distribution on the vertical loading cases have been presented in Figure 4.6. Looking again at the region between 30 and 70 degrees, it can be seen that a decrease in velocity resulted in greater pressures on the underside of the wheel for the VL1 wheel. This is the opposite of what was observed with the centrifugal growth cases. The peak pressure value was also observed to be similar to that of the A2 wheel. This showcases the reasoning behind the increase in

lift that was observed with this wheel. However, a significant decrease in the positive pressure peak at the contact patch was observed with the VL2 wheel. This is primarily due to the significant energy loss in the flow due to the sidewalls being in such close proximity to the ground. This resulted in a reduced lift coefficient. However, this does not explain the reason for the reduction in drag.

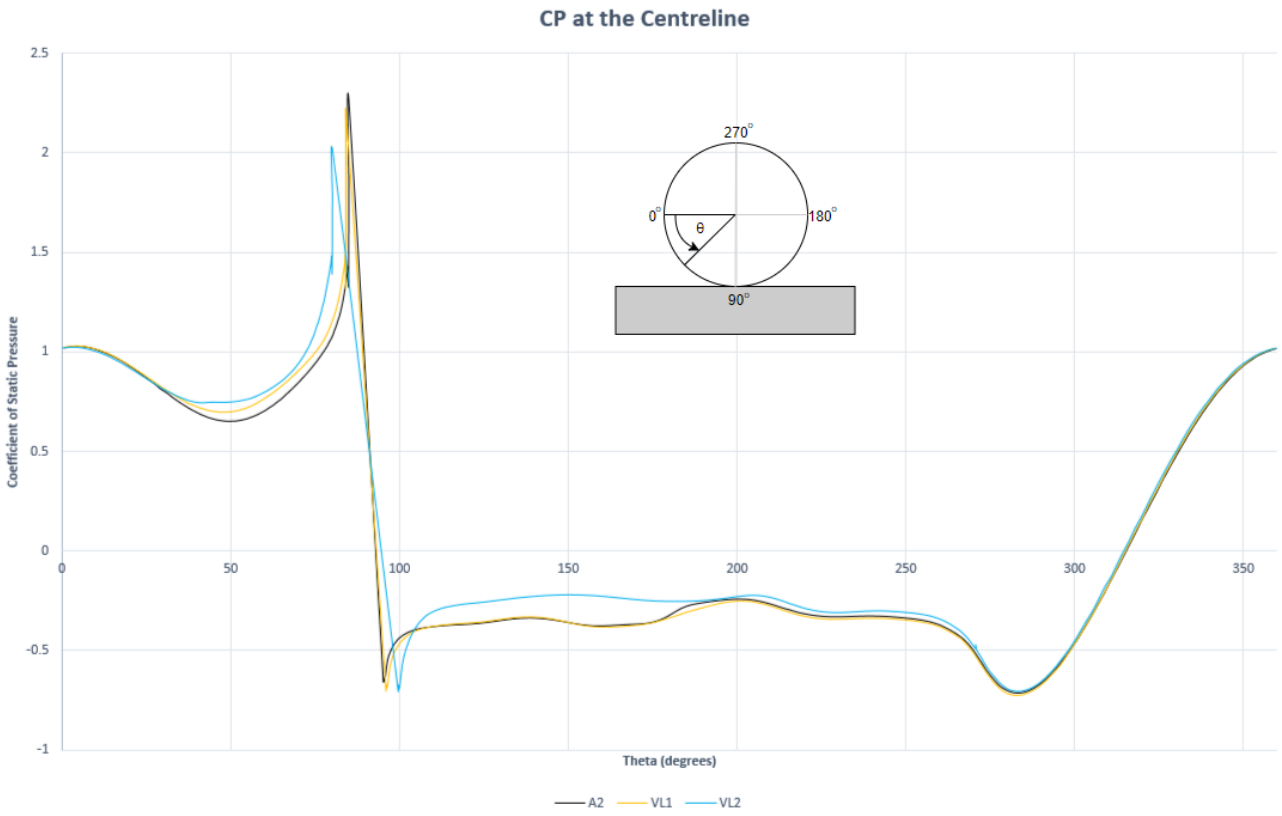

Figure 4.6: Coefficient of pressure distribution around the centreline of the increased vertical loading cases.

From 100 degrees to 180 degrees, the VL2 wheel showcases variations different from all other wheels. There is significantly less pressure loss directly behind the contact patch for the VL2, a possible reason for the reduction of drag for this wheel. The reasoning for this pressure drop is investigated in later sections. Similar to the centrifugal growth cases, the vertical loading cases showcased no variation in the flow separation point.

4.3.3 Flow Field Observations

The VL1 wheel showcases earlier formation of the two primary vortices compared to the A2 wheel. This results in them being wider initially but carrying less energy, causing them to decay earlier. Interestingly, these vortices are either not formed at all or carry significantly less energy in the VL2 wheel. It can be seen that this wheel experiences a much greater pressure deficit on either side of the

contact patch than all other wheels tested. This pressure deficit is primarily due to the close proximity that the sidewalls have to the ground, due to an increase in vertical load, causing the flow to accelerate.

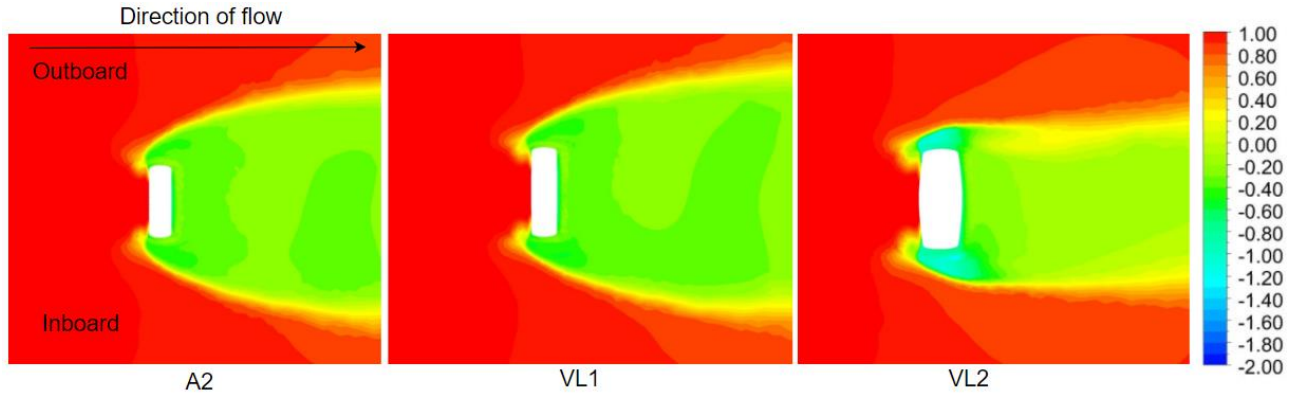

Figure 4.7: Variations in the wake structure due to increased vertical loading at z=0.01D.

This results in the early separation of flow at the sidewalls of the wheels, restricting the formation of the two main vortices at the contact patch. This results in the formation of the narrow wake structure. Due to the lack of energy in the vortices in this region, the flow travels in the direction where low pressures are present, which is directly behind the wheel. This wake structure also explains the nature of the static pressure distribution seen in Figure 4.8.

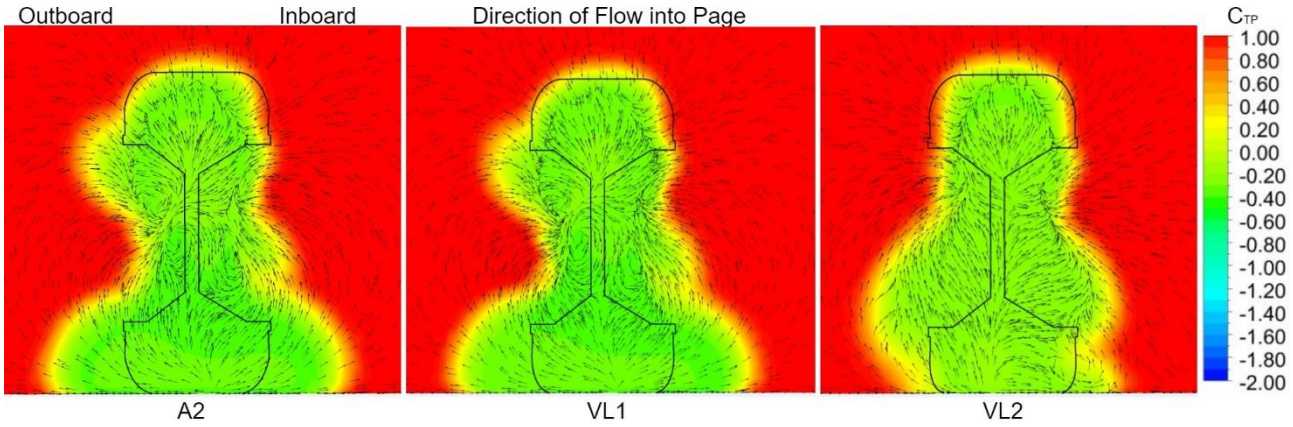

Figure 4.8: Variations in the wake structure due to increased vertical loading at x/D = 0.52.

Travelling further downstream, it can be seen that the VL1 wheel forms lower and wider wake, given its wider contact patch and the fact that this wheels primary vortices contain less energy. The largest variance seen was again with the VL2 wheel. The lack of energy in the primary vortices being formed on this wheel is apparent as the width of the wake is proportional to the width of the wheel as well as the fact that the vectors show no form of rotation. Another noticeable change is the flow through the hubs and the wake structure being created from them on the outboard side being lower than the other wheels. However, it cannot be confirmed that this is the result of the changes made to the sidewall. This is due to the fact that many unsteady flow structures are present on wheels and this change in

the flow around the hub could potentially be down to the fact that this was a steady state RANS simulation. Therefore, an unsteady simulation of this geometry would be advised.

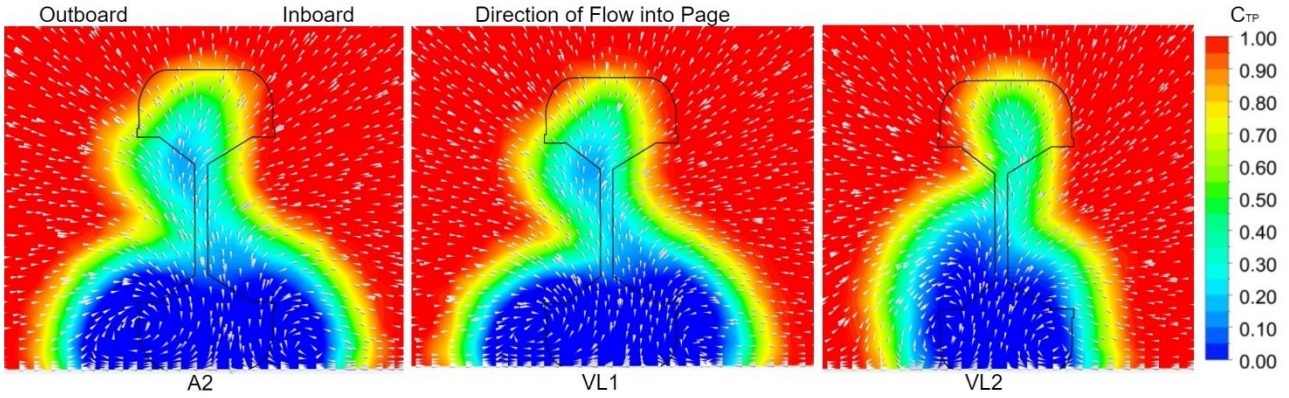

Figure 4.9: Variations in the wake structure due to increased vertical loading at x/D = 1.2.

Conversely, the VL1 wheel showcased significantly weaker vortex structures, due to less energy being present. The lack of energy in these primary vortices is again apparent in the VL2 wheel, with the flow showcasing no rotational velocity.

The height of the wake for the VL1 wheel did not vary in comparison to the A2 wheel, this showcases the little variance these wheels had in drag coefficient. However, it can be seen in the VL2 wheel, that the height of the wake has not significantly changed from the location x/D = 0.52, showcasing how influential the primary vortices are in shaping the wake structure as we move further downstream.

4.4 The Effect of Asymmetric Loading

4.4.1 Lift and Drag comparison

The AS1 wheel showcased no accountable variations in lift or drag when compared to the A2 wheel. This is presented in the table below. Given that the AS1 wheel essentially has the inboard side of the VL1 wheel and the outboard side of the CG1 wheel, variations in lift and drag were not expected. This is because, as demonstrated in earlier sections, the compression and stretching of the sidewalls influence the flow structures in an opposite manner. This results in the deformation of the AS1wheel essentially cancelling the effects of the other out when looking at force data.

Table 4.3: Lift and drag comparison of the asymmetric loading case.

Wheel	Drag Coefficient	Lift Coefficient	% Variance Drag	% Variance Lift
A2	0.5688	0.1821	N/A	N/A
AS1	0.5728	0.1842	-0.71%	-1.16%

4.4.2 Pressure Distribution Comparison on the Wheel Surface

Similar to the force data presented, the AS1 wheel showcased no measurable variation in the pressure distribution at the centreline. The reasoning for this is the same as what was given for the force measurements, with the deformation on either side essentially negating the effects of the other.

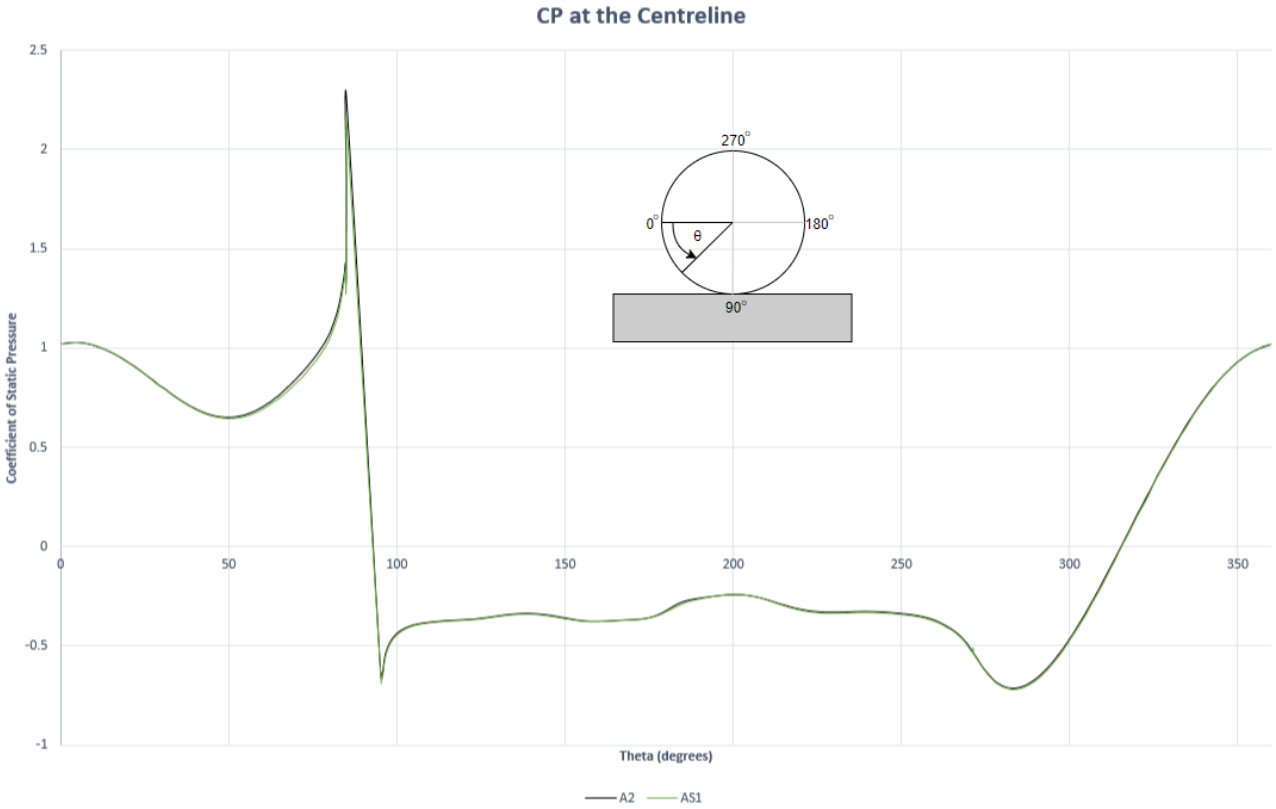

Figure 4.10: Coefficient of pressure distribution around the centreline of the asymmetric loading case.

4.4.3 Flow Field Observations

Unlike the pressure distribution and force measurements above, the AS1 wheel did showcase variations in the flow structures associated with the contact patch.

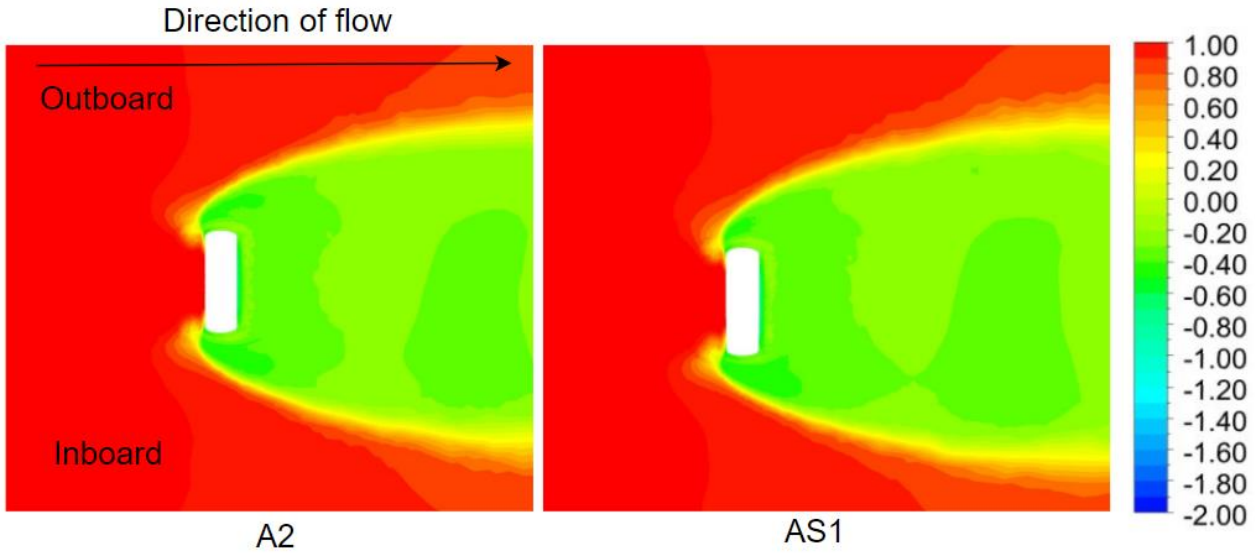

Figure 4.11: Variations in the wake structure due to asymmetric loading at z=0.01D.

There are subtle changes that can be seen with the AS1 wheel. It can be seen that there is a slight skewness seen in the flow behind the contact patch. The formation of the vortex on the inboard side is earlier than in the A2 wheel and the outboard side vortex forms later than the A2 wheel. This is consistent with what was seen with both the CG1 and VL2 wheels. However, both the inboard and outboard side of the AS1 wheel closer resemble that of the A2 wheel than either the VL1 and CG1 wheels, suggesting that the inboard and outboard side geometries affect the flow formation of the opposite side.

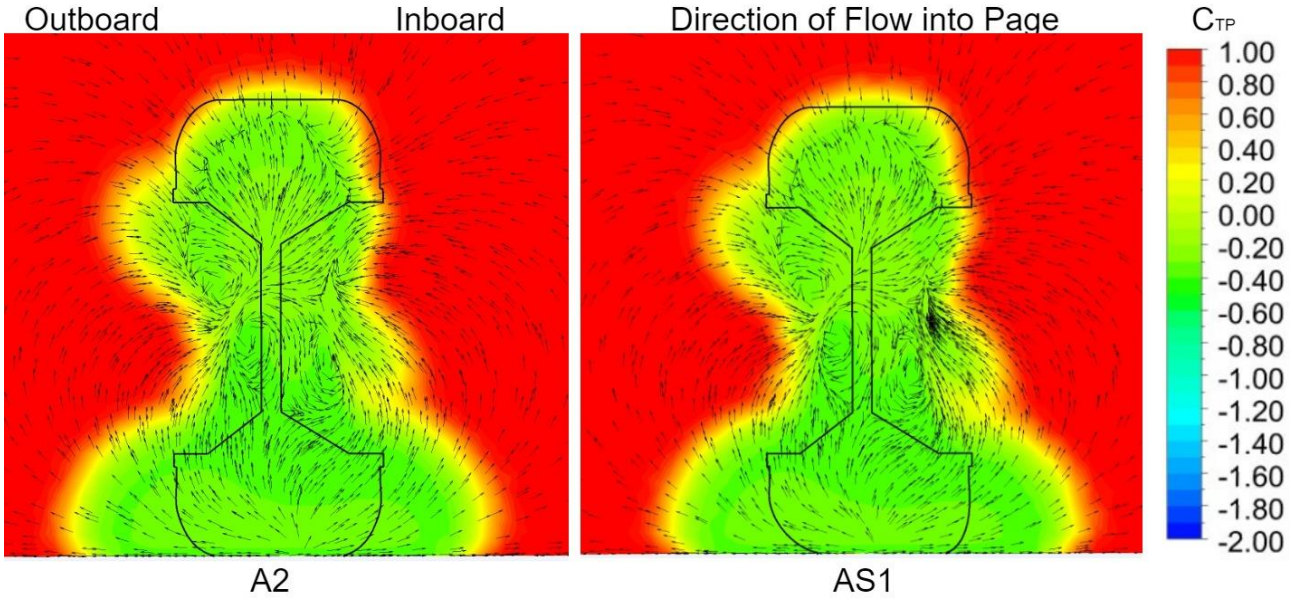

Figure 4.12: Variations in the wake structure due to asymmetric loading at x/D = 0.52.

As the flow moves further downstream, the AS1 wheel showcases the structures observed with the CG1 and VL1, as seen in Figure 4.13.

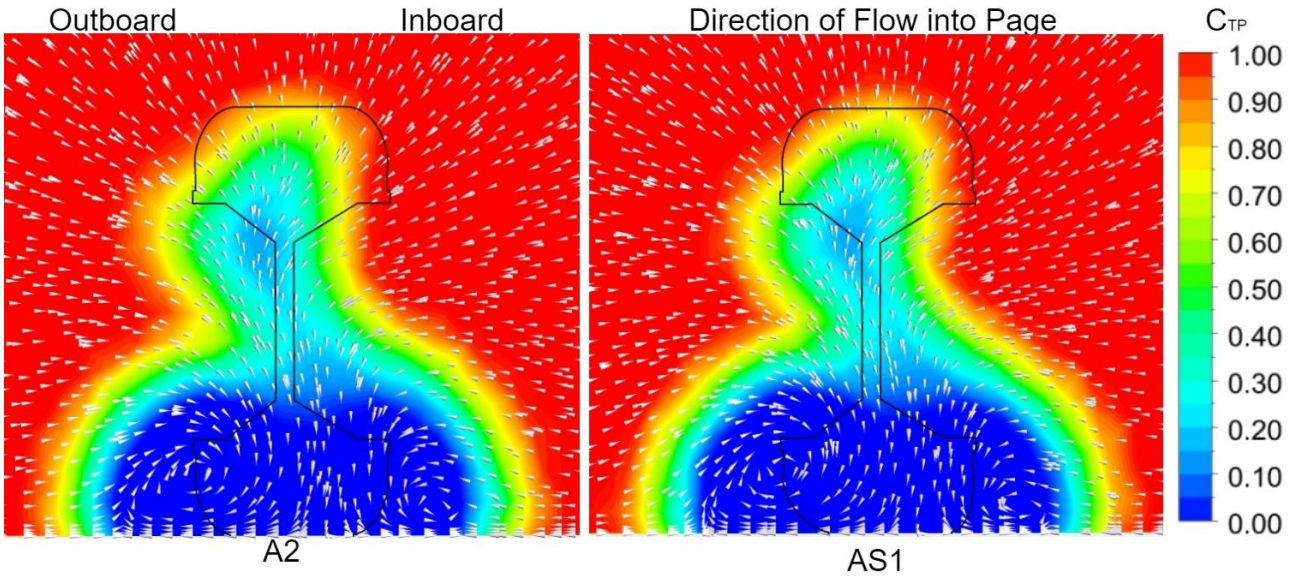

Figure 4.13: Variations in the wake structure due to asymmetric loading at x/D = 1.2.

It is evident that the outboard vortex showcases more strength than the inboard vortex, due to the stretching and compressing sidewalls respectively. It is also apparent that at the top of the wake, the structure skews towards the inboard side, due to the lack of energy in the inboard vortex. However, it can be seen that neither the outboard nor inboard vortices share the strength of either the CG1 or VL1 wheel. It is evident that the outboard vortex of the AS1 wheel is weaker than the outboard vortex of the CG1 wheel. The opposite is the case for the inboard side, with the AS1 vortex being stronger than the VL1 vortex. This suggests that sidewall variations affect the formation of the vortices on the opposite side of the wheel.

4.5 Summary of the Effects of Tyre Deformation on Key Flow Structures

To illustrate the effects that the tyre deformation had on the flow structures associated with the wheels with greater clarity, an iso-surface of the A2 and AS1 wheels with a constant total pressure of 0.3 have been with different viewing points has been showcased in Figure 4.14. The key flow structures have been identified. These structures are i) inboard primary vortex downstream, ii) outboard primary vortex downstream, iii) outboard primary vortex near the contact patch, iv) inboard primary vortex near the contact patch, v) top of the wake and vi) separation point.

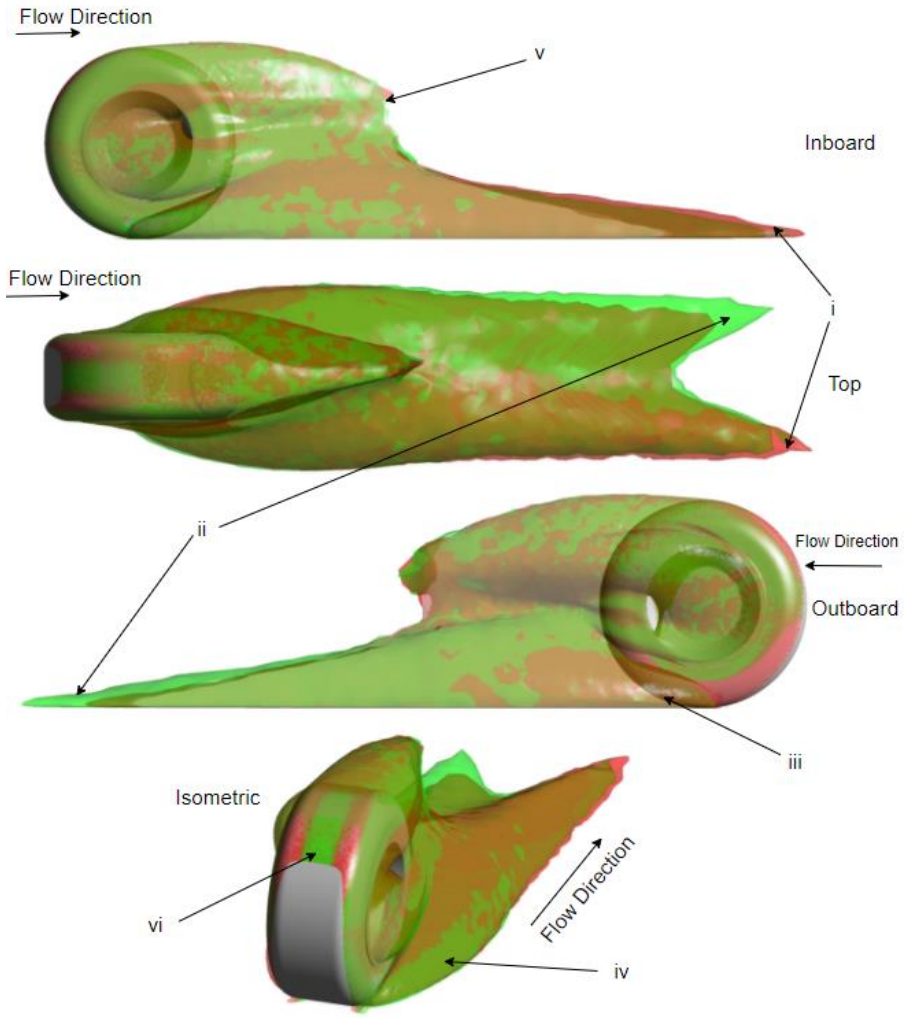

Figure 4.14: Iso-surface of coefficient of total pressure equal to 0.3 on the A2 (red) and AS1 (green) wheels.

The deformation at the sidewalls near the contact patch had no significant effect on the separation point over the top of the wheel, this resulted in minimal changes in the wake structure immediately behind this top surface, as can be visualised with all four views. These findings are consistent with what was seen with the surface pressure distribution. The centrifugal growth of the sidewalls on the outboard side caused an initial lower and narrower vortex to be created. However, this vortex carried more energy and was able to keep its structure for a greater distance, resulting in a taller, longer and wider wake structure seen in the top and outboard views. The increase in loading on the sidewalls on the inboard side had the opposite effect. Initially creating a taller and wider vortex, but the lack of energy resulted in this vortex dispersing faster than the standard A2 wheel.

Extreme loading of the sidewalls restricted the formation of the two primary vortices. This is due to the sidewalls being in a position to take energy out of the flow that is travelling towards the contact patch.

5 Conclusions and Future Work

5.1 Conclusion

The simulations that were conducted showcased that tyre deformation due to operating conditions does have significant aerodynamic consequences on the flow structures associated with wheels as well as its overall lift and drag.

The centrifugal growth of the sidewalls of the CG1 and CG2 wheels decreased the width of the tyre contact patch significantly whilst also slightly decreasing the length. These changes to the contact patch did influence the width of the wake produced by these wheels, creating much narrower wake regions. However, the most significant effect of the centrifugal growth of the sidewalls was how the increase in the area underneath the wheel energised the two primary vortices due to the increase in velocity of air entering this region. The strength of these vortices impacts any component that is situated behind the wheel. These highly energised vortices can potentially be utilised by aerodynamic devices on vehicles, improving the overall aerodynamic performance. As the sidewalls were grew more, these vortices became more energised. However, no limit was found on how energetic the two primary vortices can become.

The CG1 and CG2 wheel both saw reductions in drag and lift. The reduction in drag can be attributed to the straighter sidewalls, creating narrower wake structures. These findings are consistent with Diasinos, who showcased that the reduction in the side of the wake due to contact patch step height, resulted in a decrease in lift and drag [11]. The geometric change disturbed the airflow around the wheel less than the standard A2 wheel, as was seen by the narrower wake structure at the top of the wheel. The reduction in lift can be explained by the increase in the area underneath the wheels. This increase in the area results in an increase in velocity of air in this region, causing lower pressures. This creates a net loss in overall lift produced by the wheel. This reduction in lift and drag from the CG1 and CG2 wheels suggests that running vehicle with higher tyre pressures improves the aerodynamic efficiency.

The increased vertical loading on the VL1 wheel did have an opposite effect on the flow structures of the wheel. It was seen that the reduction of the area under the wheel decreased the mass flow rate of air that is used to energise the two primary vortices, resulting in weaker vortices being formed. However, the wider contact patch created an initial wider wake region at the contact patch, but the

lack of energy quickly dissipated these flow structures downstream. The flow structures associated with the VL2 wheel saw far more significant changes. The extreme sidewall compression had a choking effect on the flow leading up to the contact patch. Enough energy was taken out of the flow before it reached the contact patch, thus restricting the formation of the two primary vortices.

The VL1 wheel saw no changes in overall drag, however, it did see an increase in lift. The increase in lift can be attributed to the opposite reason of the CG1 and CG2 wheels. The reduced area underneath the wheel reduced the air flow rate into this region, causing higher pressures. These higher pressure were not seen in this region for the VL2 wheel, however. Due to the amount of energy taken out of the flow in this region, significantly lower pressure was seen around the contact patch. This resulted in an overall loss of lift. The reduction in drag seen in the VL2 wheel can be attributed to the early separation seen near the contact patch. This resulted in a much narrower wake being formed, signifying a reduction in drag. Another potential contributor to the reduced drag could be the flow that was seen through the hubs. The vortices that are formed from the hub were much lower on the VL2 wheel, however, it cannot be confirmed that this is a direct response to the tyre deformation, as the flow around the hubs is highly unsteady. An unsteady simulation is required to confirm or deny this.

The separation point over the top of the wheel did not vary by a considerable amount throughout each case. The separation point between each case was within 5 degrees, and this is potentially due to the variations in diameter of the wheels rather than sidewall configuration.

Each of these findings was confirmed by the AS1 wheel. The AS1 wheel had the inboard sidewall of the VL1 wheel and the outboard sidewall of the CG1 wheel. It was seen that both the lift and drag of the AS1 wheel were very similar to the standard A2 wheel, suggesting that the changes on the inboard and outboard side cancelled each other. The expected variations in the flow structures were also observed. The inboard vortex was both weaker in strength and wider in size when compared to the outboard side. However, it was seen that the inboard side vortex was stronger than the VL1 inboard vortex and the outboard vortex was weaker than the CG1 outboard vortex. This suggests that the formation of each vortex is dependent on the structure of the sidewall on the opposite side of the wheel.

5.2 Recommendations for Future Work

The most direct expansion of this study would be to conduct transient simulations on deformed wheel geometries in an isolated manner. As has been discussed in previous chapters, the flow features associated with wheels are unsteady in nature. Using a transient solver would deepen the knowledge of how deformation affects key flow features on wheels given their unsteady nature.

Previous studies have been conducted on the effect that camber and yaw have on the flow structures of wheels. This study can be paired with a camber and yaw study to closer match the operating conditions of wheels [23].

Further studies can be conducted that move away from isolated wheels. It is common for vehicles to have housing for the wheels, therefore it would be interesting to see how deformation of a tyre inside a wheel housing affects it flow structures. Such a simulation would enhance the ability to use these flow structures to enhance the overall aerodynamic performance of a vehicle.

Experimental investigations can also be conducted on pneumatic tyres to validate the results showcased in this study. This experiment could utilise a method to load a tyre with a known force value whilst also capturing the geometry accurately. This would allow the experiment to not only be utilised for aerodynamic validation but could also be used for validating any computational structural analysis of tyres.

Expanding on this, structural analysis on wheels via FEA could also be used to create geometry for CFD simulations. Fluid Structure Interaction (FSI) opens many avenues for aerodynamics studies. FSI simulations on a deformable wheel create the potential to perform dynamic loading scenarios. This would allow a condition to be set up that simulates a car accelerating and then braking. FSI would allow the visualisation of the change in flow structures as this deformation increases.

References

[1] S. Diasinos, K. Dongre, J. Keogh, G. Doig and T. Barber, "Computational Analysis Comparing Aerodynamic Performance of Simplified Sedan, Wagon and SUV Automobile Configurations," in FISITA 2014 World Automotive Congress, Masstricht, 2014.

[2] T. Regert and T. Lajos, "Description of flow field in the wheelhouses of cars," Science Direct, pp. 616-629, 2007.

[3] S. Diasinos, "The Aerodynamic Interaction of a Rotating Wheel and a Downforce Producing Wing in Ground Effect," University of New South Wales, 2009.

[4] A. Morelli, "Aerodynamic Effects on the Car Wheel," ATA Review, 1969.

[5] A. Cogotti, "Aerodynamic Characteristics of Car Wheels. International Journal of Vehicle Design," Special Publication SP3, pp. 173-196, 1983.

[6] A. J. Sprot, "Open-Wheel Aerodynamics: Effects of Tyre Deformation and Internal Flow," Durham University, 2013.

[7] J. Fackrell, "The aerodynamics of an isolated wheel rotating in contact with the ground," University of London, 1974.

[8] A. P. Mears, "The aerodynamic characteristics of an exposed racing car wheel," University of Durham, 2004.

[9] P. Bearman, D. D. Beer, E. Hamidy and J. Harvey, "The Effect of a Moving Floor on Wind-Tunnel Simulation of Road Vehicles," SAE Technical Paper 880245, 1988.

[10] J. McManus and X. Zhang, "A computational study of the flow around an isolated wheel in contact with the ground," Journal of Fluids Engineering, vol. 128, no. 3, pp. 520-530, 2006.

[11] S. Diasinos, T. J. Barber and G. Doig, "The effects of simplifications on isolated wheel aerodynamics," Macquarie University, 2014.

[12] F. Malizia, H. Montarezi, P. Hespel and P. Blocken, "The influence of the rim depth to the aerodynamic performance of a wheel: a numerical study," Journal of Science and Cycling, vol. 6, no. 3, 2017.

[13] T. D. Kothalawala and A. Gatto, "Computational investigation into the influence of yaw on the aerodynamics of an isolated wheel in free air," International Journal of Computational Science and Engineering, vol. 13, no. 4, 2016.

[14] T. Hobeika, L. Lofdahl and S. Sebben, "Study of different tyre simulation methods and effects on passenger car aerodynamics," in Proceedings of the IMechE International Vehicle aerodynamics Conference, 2014.

[15] F. Wittmeier and T. Kuthada, "The influence of wheel and tire aerodynamics in WLTP," in 6th International Munich Chassis Symposium, 2015.

[16] P. Leśniewicz, M. Kulak and M. Karczewski, “Vehicle wheel drag coefficient in relation to travelling velocity - CFD analysis,” Journal of Physics, vol. 760, no. 1, 2016.

[17] A. Kremheller, M. Moore, G. L. Good, D. Sims-Williams, J. Newbon and R. Lewis, “The effects of transient flow conditions on the aerodynamics of an LCV concept using CFD and wind tunnel experiments,” Institution of Mechanical Engineers , pp. 189-201, 2016.

[18] L. Haag, M. Kiewat, T. Indinger and T. Blacha, “Numerical and Experimental Investigations of Rotating Wheel Aerodynamics on the DrivAer Model With Engine Bay Flow,” American Society of Mechanical Engineers, 2017.

[19] D. Söderblom, P. Elofsson, L. Hjelm and L. Löfdahl, “Wheel Housing Aerodynamics on Heavy Trucks,” The Aerodynamics of Heavy Vehicles, vol. 3, pp. 211-223, 2016.

[20] K. D. Marco, J. Stratton, K. Chinavare and G. VanHouten, “The Effects of Mass and Wheel Aerodynamics on Vehicle Fuel Economy,” SAE Technical Paper, 2017.

[21] L. Haag, T. Blacha and T. Indinger, “Experimental Investigation on the Aerodynamics of Isolated Rotating Wheels and Evaluation of Wheel Rotation Models Using Unsteady CFD,” International Journal of Automotive Engineering, vol. 8, no. 1, pp. 7-14, 2017.

[22] M. Kulak, M. Karczewski, P. Leśniewicz, K. Olasek, B. Hoogterp, G. Spolaore and K. Jóźwik, “Numerical and experimental analysis of rotating wheel in contact with the ground,” International Journal of Numerical Methods for Heat & Fluid Flow, 2017.

[23] W. Milliken and D. Milliken, Race Car Vehicle Dynamics, SAE International, 1st edition, 1995.

[24] F. Farroni, A. Sakhnevych and F. Timpone, “Physical modelling of tire wear for the analysis of the influence of thermal and frictional effects on vehicle performance,” Institute of Mechanical Engineers, 2016.

[25] X. Yang and O. A. Olatunbosun, “Optimization of reinforcement turn-up effect on tyre durability and operating characteristics for racing tyre design,” Materials & Design, vol. 35, pp. 798-809, 2012.

[26] R. A. Ridha and M. Thieves, “Advances in Tyre Mechanics,” Rapra Technology, 1994.

[27] A. J. Chorin, “Numerical Solution of the Navier-Stokes Equations,” Mathematics of Computation, vol. 22, pp. 745-762, 1968.

[28] J. H. Ferziger and M. Peric, Computational Methods for Fluid Dynamics, Berlin: Springer-Verlag Berlin Heidelberg, 2002.

[29] J. Keogh, G. Doig and S. Diasinos, “Flow compressibility effects around an open-wheel racing car,” The Aeronautical Journal, vol. 118, pp. 1409-1431, 2014.

[30] H. K. Versteeg and W. Malalasekera, An introduction to computational fluid dynamics: The finite volume method, Essex: Longman Scientific and Technical, 1995.

[31] T.-H. Shih, W. H. Liou, A. Shabbir, Z. Yang and J. Zhu, “A new k-epsilon eddy viscosity model for high reynolds number turbulent flows,” Computers Fluids, vol. 24, no. 3, pp. 227-238, 1995.

[32] F. Inc, “Fluent User's Guide,” ANSYS Inc, 2015.

[33] D. C. Wilcox, Turbulence modeling for CFD, La Canada: DCW Industries, 2006.

[34] F. R. Menter, “Two-equation eddy-viscosity turbulence models for engineering applications,” AIAA Journal, vol. 32, no. 8, pp. 1598-1605, 1994.

[35] K. D. Walters and D. Cokljat, “A three-equation eddy viscosity model for Reynolds-averaged Navier-Stokes simulations of transitional flows,” Fluids Eng, vol. 130, no. 12, 2008.

[36] S. M. A. Aftab, A. S. M. Rafie, N. A. Razak and K. A. Ahmad, “Turbulence model selection for low Reynolds number flows,” PLoS One, vol. 11, no. 4, 2016.

[37] F. R. Menter, R. B. Langtry, S. R. Likki, Y. B. Suzen, P. G. Huang and S. Volker, “A correlation-based transition model using local variables,” Journal of Turbomachinery, vol. 128, no. 3, pp. 413-422, 2006.

[38] J. Tu, G. H. Yeoh and C. Liu, Computational Fluid Dynamics: A practical approach, Butterworth-Heinemann, 2012.

[39] AIAA, “Guide for the Verification and Validation of Computational Fluid Dynamics Simulations,” AIAA, 1998.

[40] P. J. Roache, “Perspective: A method for uniform reporting of grid refinement studies,” Journal of Fluids Engineering, vol. 116, pp. 405-413, 1994.

[41] J. Dixon, “Tyres, suspension, and handling & Society of Automotive Engineers,” Society of Automotive Engineers, London, 1996.

[42] W. R. Stapleford and G. W. Carr, “Aerodynamic Characteristics of Exposed Rotating Wheels,” Technical Report MIRA, 1970.

Appendix A: Tyre Geometry

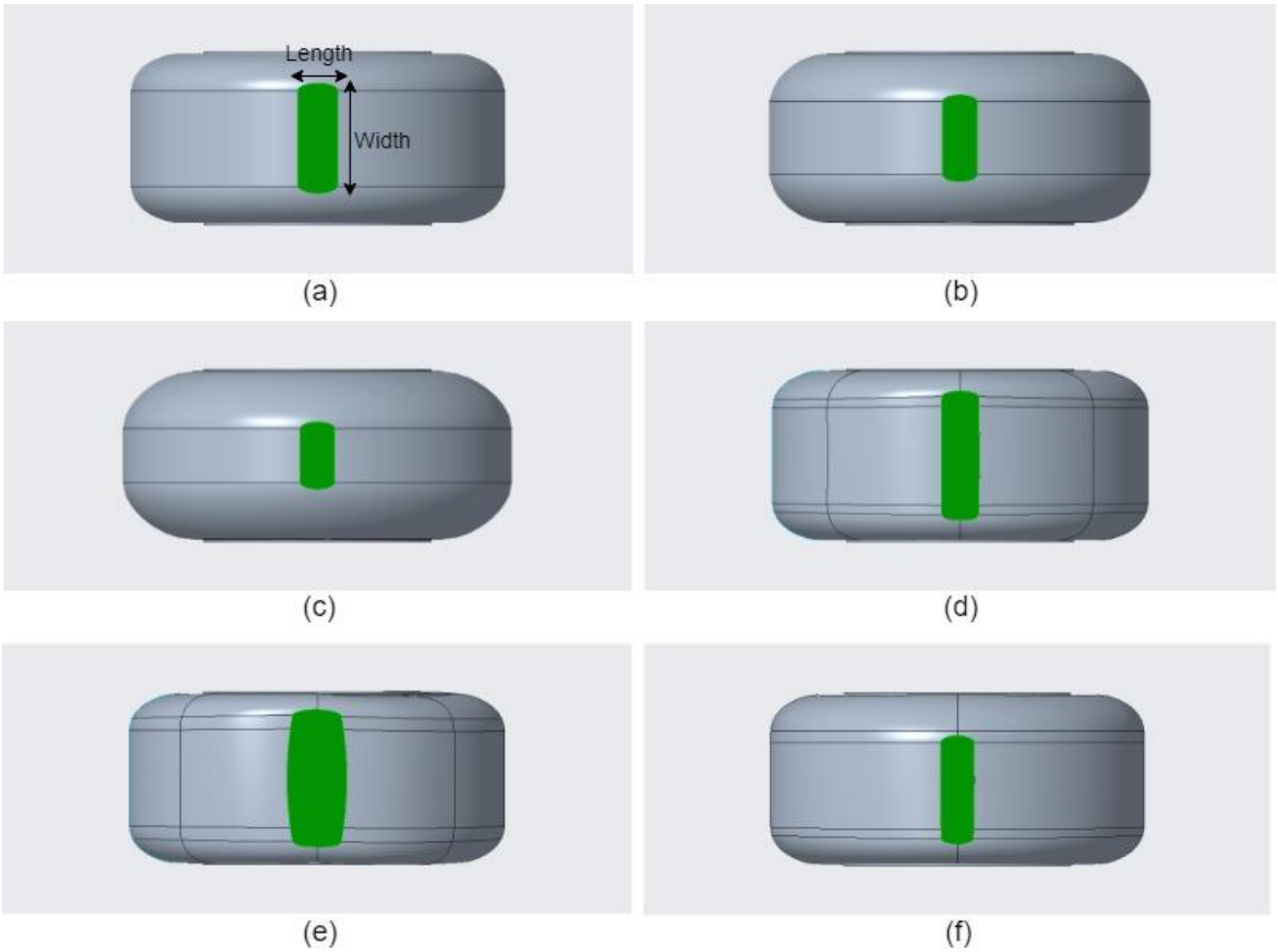

Figure A.0.1: Contact patch shape with step height of 0.002D - (a) A2 (b) CG1 (c) CG2 (d) VL1 (e) VL2 (f) AS1.

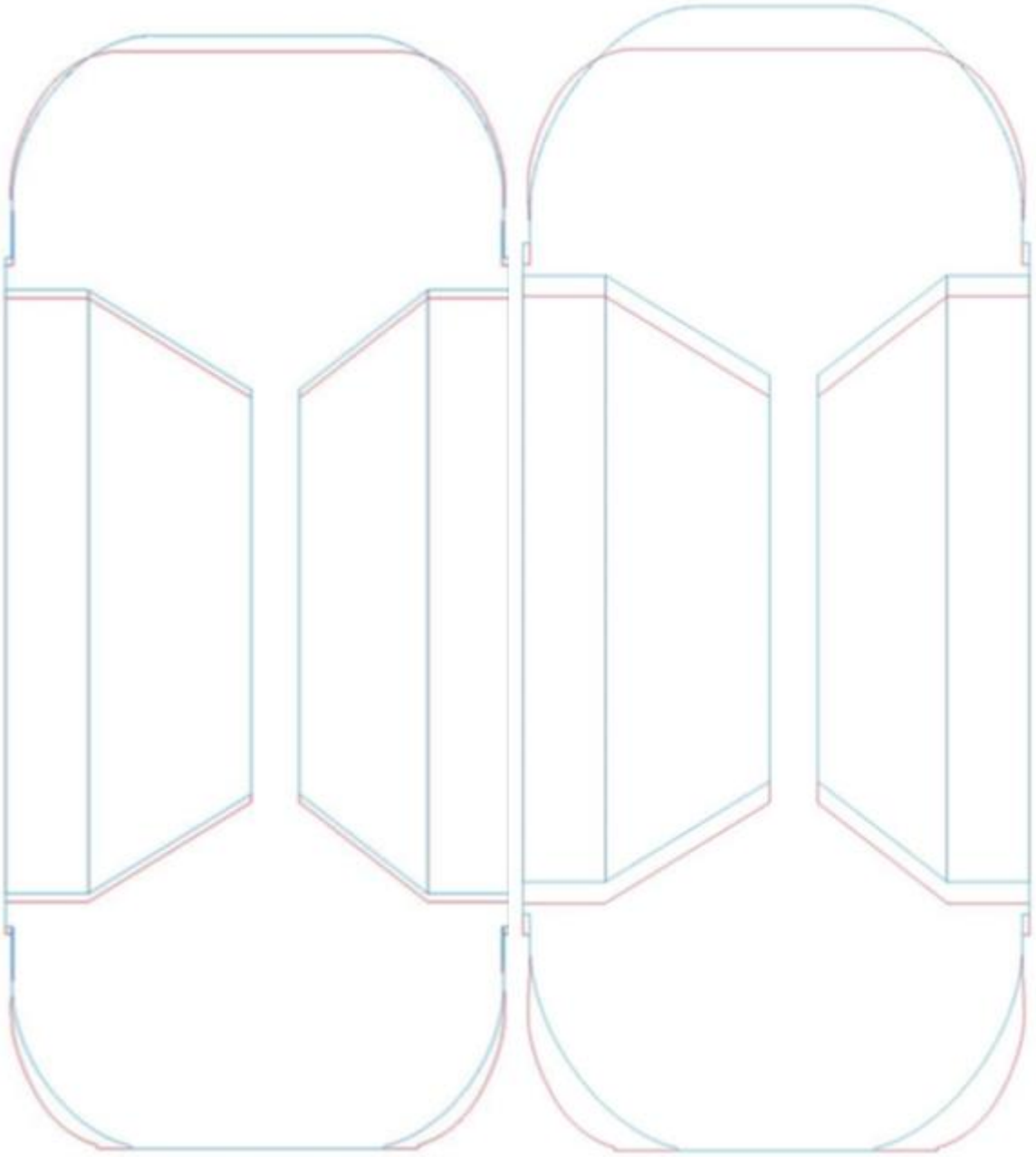

Figure A.0.2: Comparison between the CG1 (left) and CG2 (right) with the standard A2 wheel (red).

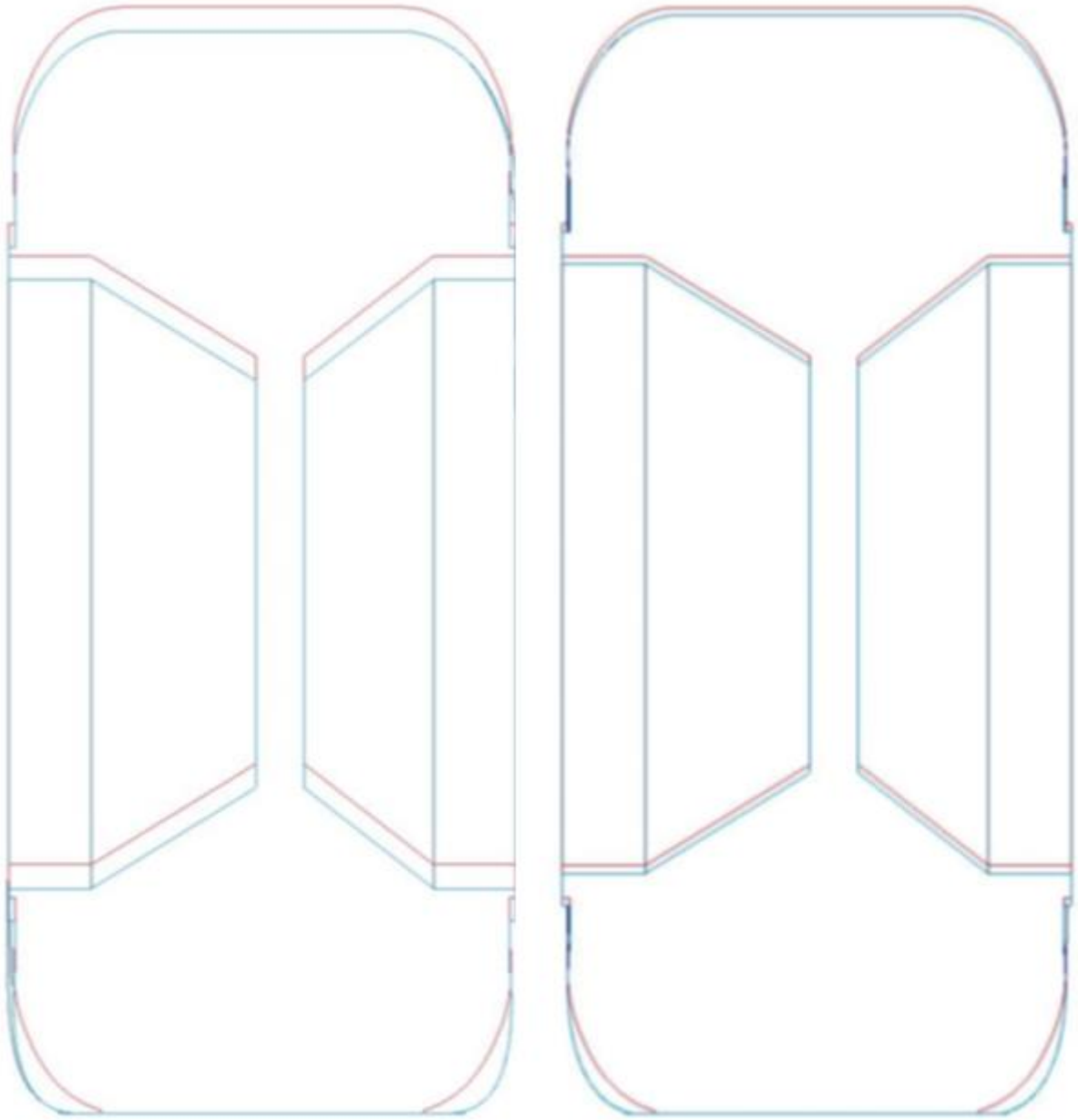

Figure A.0.3: Comparison between the VL2 (left) and VL1 (right) with the standard A2 wheel (red).

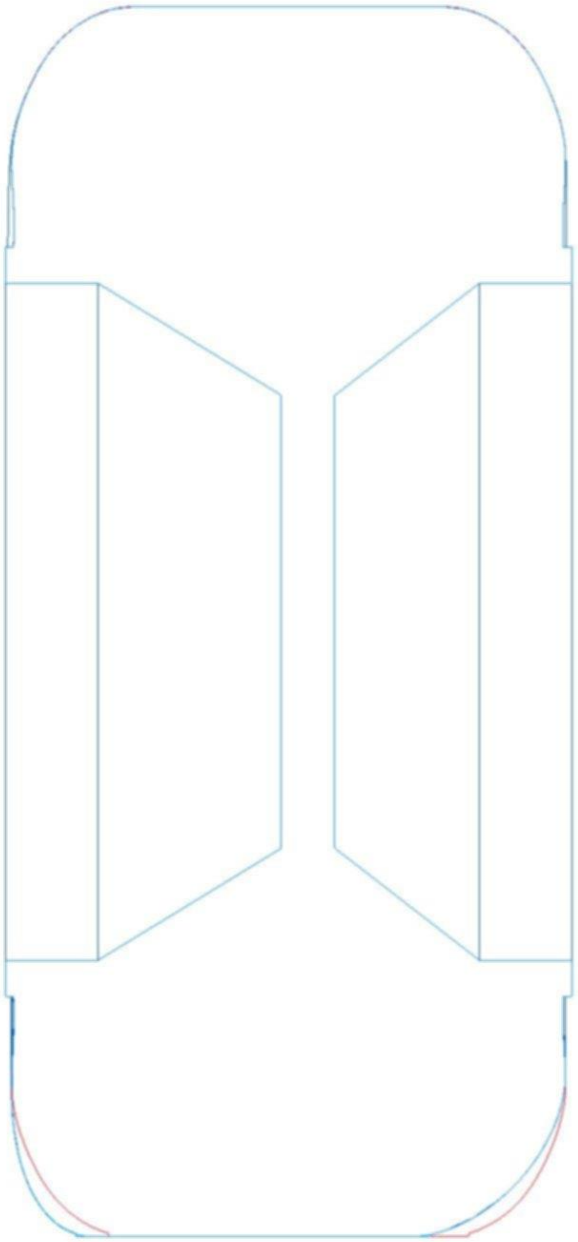

Figure A.0.4: AS1 wheel (blue) compared to Fackrell's A2 wheel (red).

Appendix B: Comparing Contact Patch Step Heights

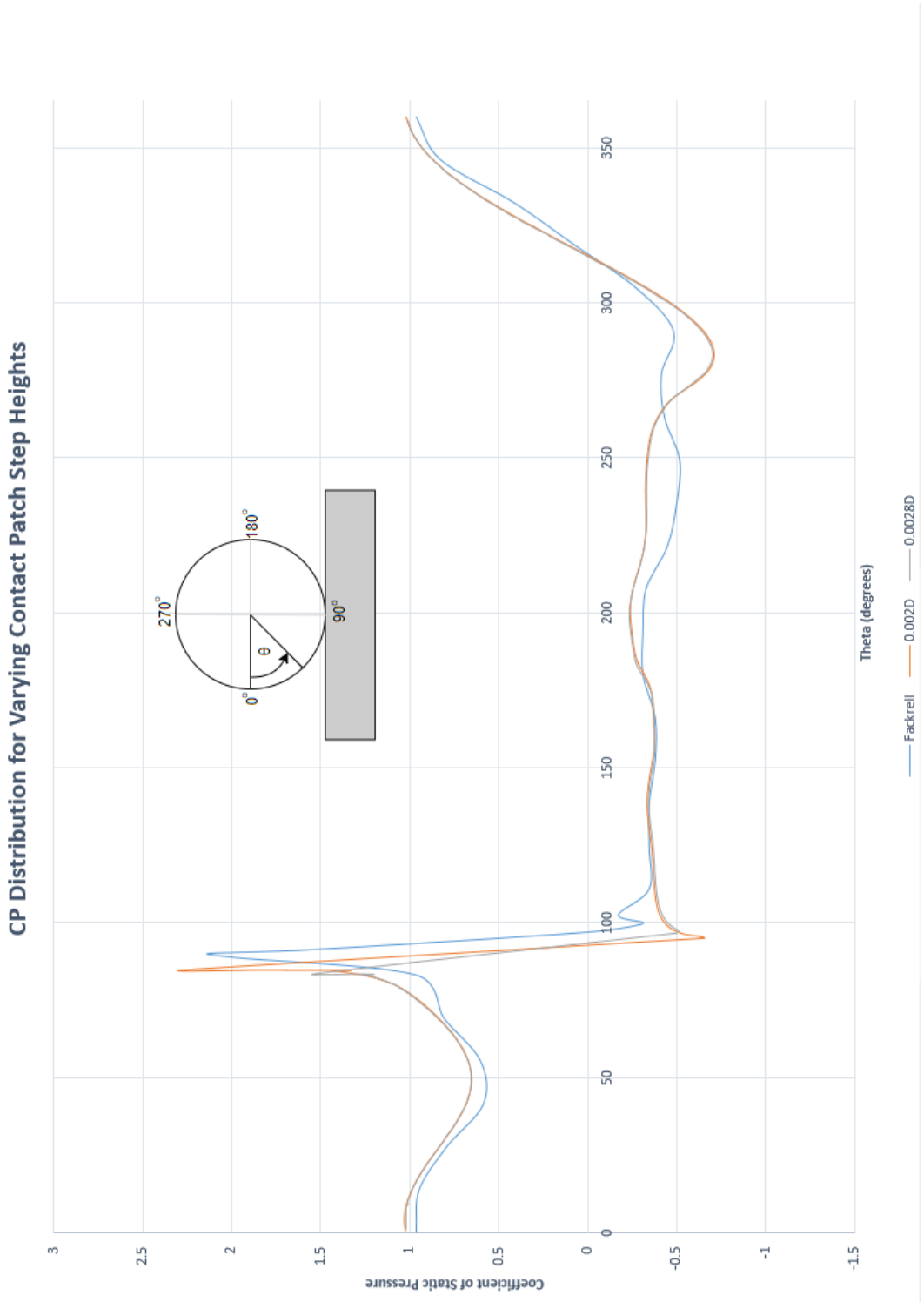

Figure B.0.1Pressure distribution at the wheel centreline for varying contact patch step heights.